Title	Structural and functional analysis of cell division proteins from methicillin-resistant Staphylococcus aureus for drug development
Author(s)	藤田, 純三
Citation	大阪大学, 2018, 博士論文
Version Type	VoR
URL	https://doi.org/10.18910/69548
rights	
Note	

Doctoral Dissertation

Structural and functional analysis of cell division proteins from methicillin-resistant *Staphylococcus aureus* for drug development

Junso Fujita

January 2018

Department of Applied Chemistry

Graduate School of Engineering

Osaka University

Structural and functional analysis of cell division proteins from methicillin-resistant *Staphylococcus aureus* for drug development

（創薬を志向したメチシリン耐性黄色ブドウ球菌由来

細胞分裂タンパク質の構造–機能相関解析）

2018

Junso Fujita

Department of Applied Chemistry

Graduate School of Engineering

Osaka University

Preface

The study presented here has been carried out under the supervision of Professor Tsuyoshi Inoue (Osaka University) and Professor Hiroyoshi Matsumura (Ritsumeikan University) from April 2012 to March 2018 at Department of Applied Chemistry, Graduate School of Engineering, Osaka University.

The object of this thesis is to elucidate the central mechanism of bacterial cell division and to establish the structural basis for the drug design, especially against methicillin-resistant *Staphylococcus aureus*.

Junso Fujita

Department of Applied Chemistry
Graduate School of Engineering
Osaka University
Suita, Osaka
Japan

January 2018

Contents

General Introduction

Chapter 1

Structural Change Mechanism of FtsZ

Chapter 2

Unique Binding Mode of FtsZ Inhibitors and Relationship to Drug-Resistant Mutation

Chapter 3

Dynamic Behavior of FtsZ Filaments Visualized by High-Speed AFM

Chapter 4

Crystallographic and Interaction Analysis of FtsA

General Introduction

0.1. Bacterial Cell Division and FtsZ

Public health agencies, such as the World Health Organization (WHO) and the Centers for Disease Control (CDC), have released reports that caution of an impending crisis to global public health due to the rise and spread of antibiotic resistance (1, 2). Therefore, it is urgently necessary to develop new antibiotics with novel bacterial targets. This situation has been shed light on cell division (3), which is an essential phenomenon for extensive species of eukaryotes, archaea, and bacteria. In *Escherichia coli*, more than 30 proteins constitute a multiprotein complex called divisome (4). Among these proteins, the tubulin homolog protein FtsZ (Filamenting temperature-sensitive mutant Z) is widely conserved in many bacteria and archaea, and plays a central role in cell division; it assembles to form filamentous structures called protofilaments, which further associate into a ring shape (Z-ring) in the presence of guanosine triphosphate (GTP) (Fig. 0-1, left panel) (5-7). FtsZ catalyzes GTP hydrolysis, which is associated with its polymerization because the GTPase active residues are located in the opposite side of the nucleotide binding pocket (8-11). The Z-ring gradually contracts to divide a cell in half (12), but how the contraction force is generated has been remained controversial. The most potent model is that FtsZ filaments bending regulated by GTP hydrolysis generates the force. Electron microscopic study has shown that highly curved filaments are formed in the presence of GDP in contrast to straight filaments with GTP (13), and computational approach also supports this hypothesis (14). Furthermore, a series of fluorescent microscopic studies using yellow fluorescent protein (YFP) and membrane-targeting sequence (MTS)-fused FtsZ demonstrate that FtsZ can deform liposome membrane (15, 16). However, recent biochemical and microscopic studies suggest that FtsZ may not generate enough constriction force for cell division and the Z-ring is cooperated with other cell division proteins for cell wall metabolism, the alternative candidate for the force generator (17). Net FtsZ filament movement caused by polymerization at one end and depolymerization at the other end, called treadmilling, has
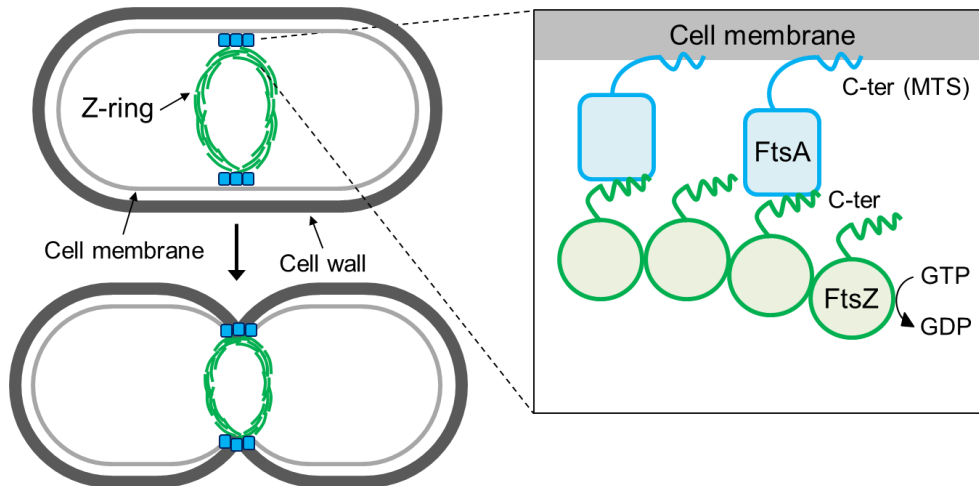
Figure 0-1. Schematic representation of FtsZ and FtsA during bacterial cell division.

been found to be important for cell wall synthesis and coupled with a GTPase activity (18, 19).

Although a number of crystallographic and biochemical studies of FtsZ derived from various species have been performed, the mechanism of the GTPase-mediated FtsZ conformational change still remains unclear. The biggest problem was that most of FtsZ crystal structures from various species show identical monomer conformation whether GTP (or its analog) or GDP is bound (20-22). Additionally, no filamentous structure is found in these crystals. On the other hand, crystal structures of FtsZ from *Staphylococcus aureus* (SaFtsZ) show apparently different features. The GDP-bound molecules align as straight filaments in the crystal, and the loop responsible for GTP hydrolysis (T7 loop) was deeply inserted into the GDP binding pocket of the adjacent molecule (23). This rigid interaction seems to be responsible for mechanism of GTP hydrolysis: the putative catalytic residues (Asp210 and Asp213) are located near the γ-phosphate of GTP analog (GTPγS), suggesting water-mediated hydrogen bonds between them, whereas no water molecules are found in the GTPγS complex because of the low resolution (2.61 Å, PDB entry: 3WGN, Fig. 0-2) (24). From these information, the conformation of SaFtsZ is considered as a tense (T) state corresponding to the straight filaments observed under GTP, and other structures are thought as a relaxed (R) state corresponding to the curved filaments observed under GDP. The identified two conformation enables prediction of the T–R conformational change mechanism. For example, the crystal structure of *Mycobacterium tuberculosis*

FtsZ (MtbFtsZ, PDB entry: 4KWE) suggests that the GTP hydrolysis induces a hinge-opening movement in FtsZ monomer, which promotes the conformational changes of FtsZ filaments (25). Crystallographic study of the SaFtsZ also suggests the FtsZ structural change between the T and R states is induced by intermolecular interactions (24). However, there is no example that both T and R FtsZ structures are determined in a single species, so the possibility cannot be excluded that the FtsZ conformation is intrinsic to the species. Some GDP-bound SaFtsZ mutants structures (altered the length of the T7 loop, PDB entry: 3WGK and 3WGL) show R-like conformations, but the result should be carefully interpreted because the heavily engineered mutants without GTPase activity are not functional (24).
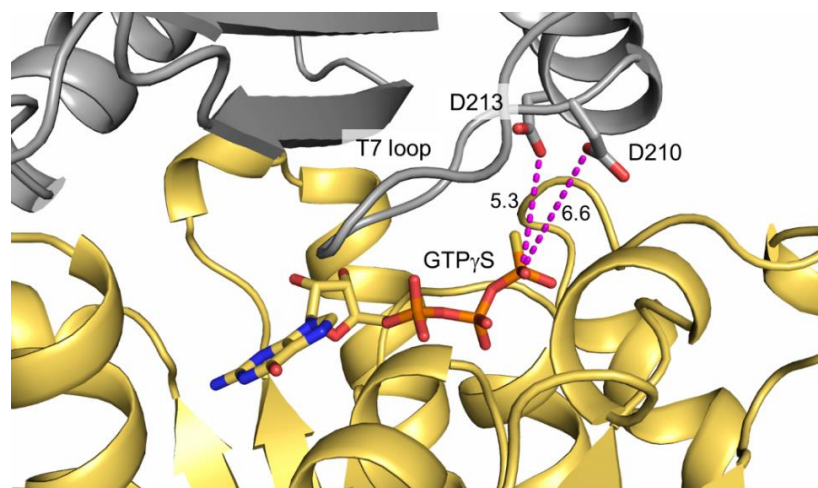

Fig. 0-2. Intermolecular interface of SaFtsZ–GTPγS complex (PDB entry: 3WGN). Upper molecule is shown in gray for clarity. The distances are labeled in Å.

Several molecular dynamics (MD) simulations have been performed to investigate the nucleotide-regulated FtsZ filament dynamics. Particularly, most previous studies have investigated how the FtsZ polymer bends by GTP hydrolysis through intermolecular interaction between neighboring FtsZ monomers (14, 26, 27). Another computational study shows that monomeric FtsZ changes the conformation from the T to R state, but the intramolecular mechanism was not analyzed in atomic detail (28). In contrast to previous studies, structural basis of intramolecular interaction during the T–R structural change has been hindered by the absence of both T and R structures of native FtsZ from a single species as described above.

0.2. Membrane Anchor Protein FtsA

The Z-ring has to be anchored to the cytoplasmic membrane, because the membrane deformation associated with the ring constriction is essential to complete cell division. FtsZ interacts with a partner protein FtsA through its C-terminal sequence (29, 30), and FtsA is also tethered to the membrane through its C-terminal amphipathic helix (MTS described above, Fig. 0-1. Right panel) (31). FtsA belongs to the actin family, which exhibits ATPase activity coupled to its polymerization (32). FtsA forms filamentous structures similar to those of actin both *in vitro* and *in vivo* (33, 34). Although recent electron cryomicroscopy and cryotomography allow the observation of three-dimensional (3D)-arranged FtsA filaments along the Z-ring (35), the role of FtsA filaments remains to be clarified. ATPase activity was exhibited in FtsA from *Bacillus subtilis* (36) and *Pseudomonas aeruginosa* (37), but it was not detected in FtsA from *Streptococcus pneumoniae* (34), *Escherichia coli* (38), and *Thermotoga maritima* (TmFtsA) (33). Fluorescence microscopic study indicates that the coexistence of YFP-fused FtsZ and FtsA* (a gain-of-function mutant of FtsA (39)) results in formation of a continuous septum in a GTP and ATP-dependent manner (40). Another fluorescence microscopic study shows that FtsZ and FtsA self-organize into rapidly reorganizing complex patterns, such as filament bundles and rings, on supported lipid bilayers (41). These results suggest that the biological role of FtsA is not merely anchoring FtsZ to the membrane but regulating FtsZ assembly. However, understanding of the molecular function of FtsA during cell division has been hampered by limited structural information of FtsA. The only crystal structure is available for TmFtsA (33, 42). The structure shows different domain architecture (1A, 1C, 2A, and 2B) compared to that of actin (1A, 1B, 2A, and 2B), and filamentous packing in the crystal (Fig. 0-3). FtsZ-binding site of FtsA was also identified by mutational study (43) and crystal structure of TmFtsA complexed with the C-terminal peptide of TmFtsZ and solution NMR studies (33). In order to extend this knowledge to other species-derived FtsA, further structural studies is required, but other FtsA often needs refolding in a purification step and seems to be difficult to prepare high purity and homogeneity sample for crystallization (37, 38).
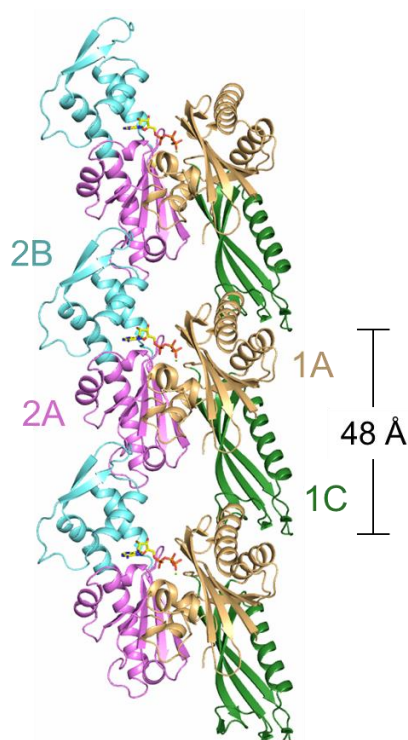
Figure 0-3. TmFtsA–ATPγS filament in the crystal (PDB entry: 4A2B). Domains 1A, 1C, 2A, and 2B are colored in light orange, green, pink, and cyan, respectively.

0.3. Development of FtsZ Inhibitors

Both FtsZ and FtsA are highly conserved and essential for cell division and viability in many bacterial species, and higher eukaryotes including human lack these proteins. These facts make them attractive targets for the development of antibacterial agents against pathogenic bacteria such as methicillin-resistant *Staphylococcus aureus* (MRSA). Especially FtsZ, a central player in bacterial cell division, has been considered to be a potent target, and many FtsZ-inhibitors, such as alkaloids, polyphenols, taxanes, nucleotide analogs, and benzamide derivatives, have been developed so far (44). However, structural information is extremely limited; only two kinds of FtsZ crystal structures complexed with its inhibitors have been determined. One is *Aquifex aeolicus* FtsZ (AaFtsZ) complexed with 8-morpholino-GTP (PDB entry: 2R75, Fig. 0-4A), a C8-substituted GTP analog (45). The other is SaFtsZ with PC190723 (PDB entries: 3VOB and 4DXD, Fig. 0-4B) (23, 46), a benzamide derivative developed from the starting compound 3-methoxybenzamide (Fig. 0-4C) (47). PC190723 binds in a cleft opened only in the T state, suggesting that it works as an allosteric inhibitor by fixing FtsZ

5

conformation to the T state. PC190723 exhibits antibacterial activity against *Bacillus subtilis* and *S. aureus* including MRSA, and does not inhibit the growth of human hepatocytes (48). PC190723 shows the tendency of stabilizing FtsZ protofilaments and increasing its GTPase activity, and it also allows polymerization at lower FtsZ concentration (49, 50). Although PC190723 is the best-known inhibitor against MRSA and commercially available, the clinical usage of the compound has been hindered by its poor solubility and formulation properties. Furthermore, several MRSA strains exhibiting the resistance against PC190723 have been isolated, and several kinds of FtsZ mutations, such as G193D, G196S, G196A, G196C, N263K, and L200F, were identified (46, 48, 51).
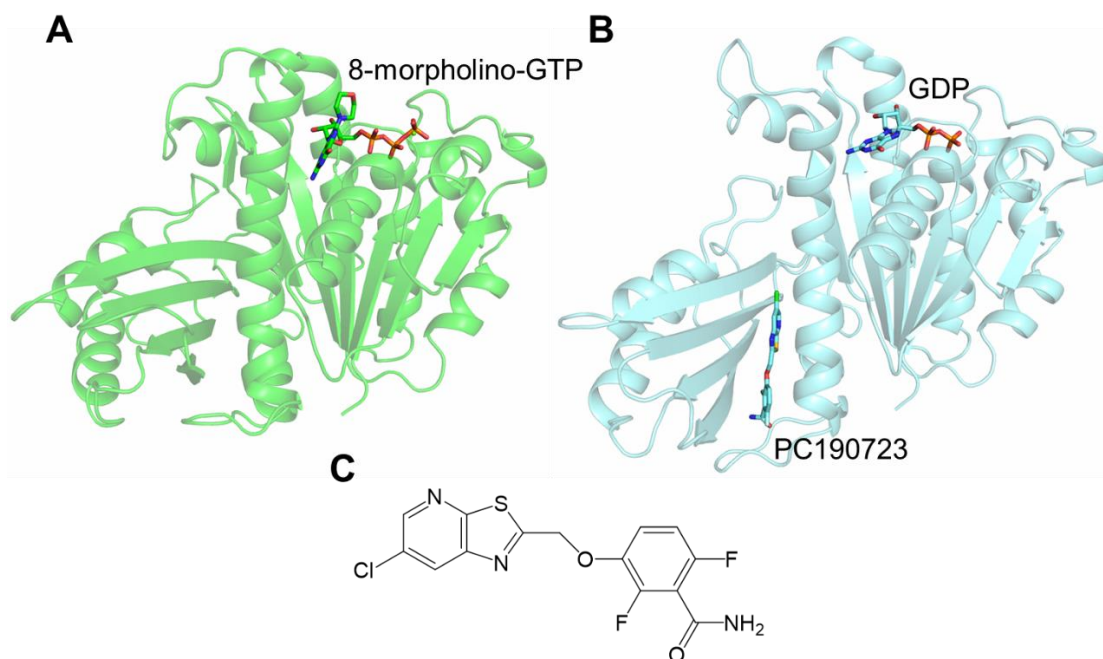
Figure 0-4. The inhibitors crystallized with FtsZ. (A, B) Overall crystal structures of AaFtsZ–8-morpholino-GTP (A, PDB entry: 2R75) and SaFtsZ–PC190723 complex (B, PDB entry: 4DXD). (C) Chemical structure of PC190723.

0.4. Outline of this Thesis

This thesis aims to clarify the central molecular mechanism of bacterial cell division by performing structural and functional analysis mainly by X-ray crystallographic analysis of SaFtsZ and FtsA from *S. aureus* (SaFtsA). Another significant purpose of this study is to establish a structural basis for new

drug development against MRSA.

In Chapter 1, the structural change mechanism of FtsZ was discussed. The author determined the structures of non-mutated SaFtsZ corresponding to the T and R state conformations in a single crystal and proposed the T–R structural change mechanism. Enhanced sampling MD simulation performed by co-workers predicted the transient structure and identified important interactions for the conformational change. Crystallographic analysis and conventional MD simulations of the mutant also supported these results.

Chapter 2 describes binding modes of the novel FtsZ inhibitors and their relationship to drug resistance mutation. The author reported the crystal structures of SaFtsZ complexed with several inhibitors developed by collaborators. Unlike previous structures, all the inhibitors in this study showed a novel bent conformation, which allowed us to identify a new inner hydrophobic pocket and to further optimize the inhibitor structures. The author also determined the crystal structure of one of the common drug resistant mutants in complex with the valid inhibitor, and revealed that the existence of bromo group and the enhanced structural flexibility of the inhibitor are significant factors for overcoming the drug resistance mutations in SaFtsZ.

In Chapter 3, dynamic behavior of FtsZ filaments and the effect of the inhibitors were investigated by high-speed atomic force microscopy (AFM). High frame rate (1 frame s^{-1}) enables visualization of the filament formation and dissociation process. Straight and curved filaments were predominantly formed in the absence and presence of the inhibitors, respectively. The difference of the filament shapes reflects that of the inhibitor activities.

Structural characterization of SaFtsA was performed in Chapter 4. The author established the way to express, purify, and crystallize SaFtsA. The crystal structure showed twisted antiparallel filaments in contrast to the straight filaments of TmFtsA. A hairpin region shows different orientation compared to that of TmFtsA because of the less hydrogen bond interaction. Additionally, the author performed SaFtsZ–FtsA interaction assays to find the importance of SaFtsZ C-terminal Arg-rich region. This unique interaction can explain the stability of SaFtsZ–FtsA complex *in vitro*.

Chapter 1

Structural Change Mechanism of FtsZ

1.1. Introduction

A number of accumulated biochemical, microscopic, and structural studies offers a basic GTPase-assembly cycle of FtsZ (Fig. 1-1). FtsZ assembles to form straight protofilaments in the presence of GTP. The GTPase active site formation between two molecules in the filaments leads to GTP hydrolysis. Structural changes by GTP hydrolysis (maybe release of inorganic phosphate) results in filament bending. The curvature of FtsZ filament decreases the binding affinity with neighboring molecules, which promotes dissociation to the monomer. Then GTP-GDP exchange recovers the first state. As mentioned in section 0.1, the mechanism of FtsZ T–R conformational change has been proposed based on the crystal structures (24, 25). However, the discussion is based on the structures of FtsZ from different species or heavily-engineered (shortened T7 loop) FtsZ mutants without GTPase activity. The crystal structures of non-mutated single species FtsZ in both T and R states must be helpful for further understanding the T–R structural change mechanism in atomic detail.
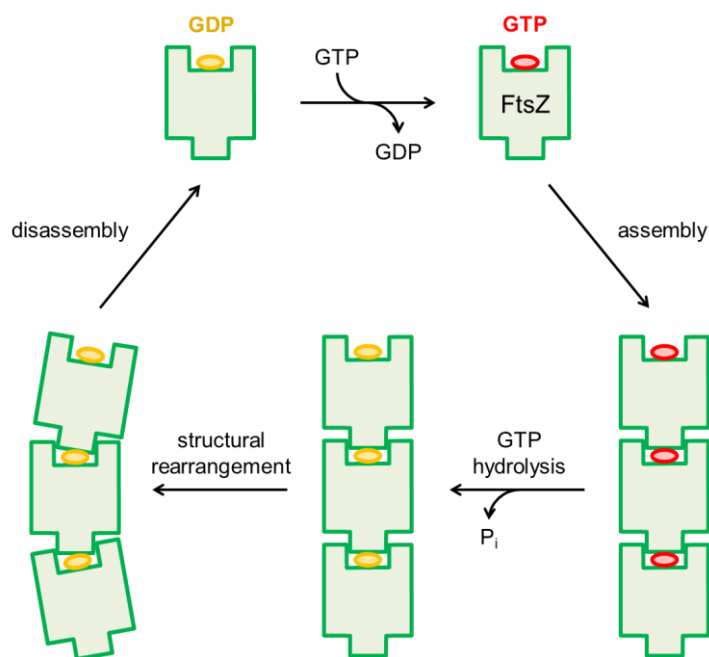

Figure 1-1. Schematic representation of FtsZ GTPase-assembly cycle.

Both T and R structure in a single species must be also useful for MD simulation. My co-workers have proposed an computational methods called the Parallel Cascade Selection MD (PaCS-MD) for enhancing the structural change and generating the pathway using two structures as an initial and final structure (52). In PaCS-MD, multiple short-time MD simulations are started from the initial structure. Then resulting many snapshots are compared to the final structure, and appropriate snapshots are selected as the structures that have high potential to change the conformation. To enhance the structural changes, the cycle between selection of appropriate initial structures and restarting of short-time MD simulations from the selected snapshots is repeated. Regenerations of initial velocities in restarting short-time MD simulations might provide sufficient kinetic energies for overcoming free energy barriers, efficiently inducing the structural changes compared to a long-time MD simulation (53).

Here, the author started from structure determination of SaFtsZ in the R state. Unexpectedly, SaFtsZ was crystallized as two conformations in the same crystal, and they were found to adopt the T and R state conformations. Several key features were identified, and a putative mechanism of the structural change was proposed. PaCS-MD simulations was applied to the T (initial) and R (final) structures by the co-workers to support and further investigate the mechanism. A transient structure generated by PaCS-MD showed a unique hydrogen bond between the side chain of Arg191 and the main chain of Arg29, which was responsible for the structural change mechanism. Therefore, the author focused on Arg29 and mutated this residue to alanine, and determined the crystal structure of the R29A mutant of SaFtsZ. The mutant also showed T and R state-like conformations, but these conformations included slight but important structural changes compared to those of WT. Conventional MD simulations of the R29A showed increased structural flexibility in both T and R conformations, suggesting that Arg29 acts as a conformational switch.

1.2. Materials and Methods

1.2.1. Cloning, expression, and purification of SaFtsZ wild-type and R29A mutant

The globular GTPase enzymatic domain of *ftsZ* gene (amino acid residues 12–316) from

methicillin-resistant *S. aureus* (strain MRSA252, Uniprot entry: Q6GHP9) was amplified from the constructed full-length *ftsz* gene inserted into pColdI vector (TAKARA BIO) (see section 4.2.1.) using KOD -plus- DNA polymerase (TOYOBO) and the following primers: forward, 5'-GGTAGGCATATGGCGACTTTAAAGGTCATTGGTGTAGGTGG-3', reverse, 5'-GAATTCGGATCCTTAATCAAAACCAGTTGCAATAACTGTTACAACAATCTC-3', and was subcloned into a modified pColdI vector, whose Factor Xa protease cleavage site (IEGR) was replaced into continuous *PstI* restriction site and tobacco etch virus (TEV) protease site (LQENLYFQG) via *NdeI* and *BamHI* sites. The resulting plasmid contains additional N-terminal extra residues of MNHKVHHHHHHLQENLYFQGHM before Ala12 of SaFtsZ. The plasmid was transformed into *E. coli* DH5α strain and extracted with QIAprep Spin Miniprep Kit (QIAGEN). Desired plasmids were selected by sequencing. The selected plasmid was transformed into *E. coli* BL21(DE3) strain and the cells were cultured in Luria–Bertani (LB) medium supplemented with 100 μg ml^{-1} ampicillin at 37 °C until the optical density at 600 nm reached 0.5. After the addition of 0.5 mM isopropyl β-D-1-thiogalactopyranoside (IPTG), cultivation was continued for 24 h at 15 °C. Cells were harvested by centrifugation for 20 min at 9000×g and 4 °C, and immediately stored at −80 °C. Cell pellets were resuspended in lysis buffer (50 mM Tris-HCl pH 7.5, 300 mM NaCl, 20 mM imidazole), and lysed with an EmulsiFlex-C3 homogenizer (Avestin). The suspension was ultracentrifuged for 30 min at 100,000×g and 4 °C. The supernatant was filtered by a 0.45 μm syringe filter (Sartorius) and loaded onto a 5 ml HisTrap HP column (GE Healthcare). The protein was eluted by a 45–310 mM imidazole gradient. Fractions containing the desired protein were dialyzed against dialysis buffer (50 mM Tris-HCl pH 7.5) for 3 h at 4 °C. TEV protease digestion reaction for hexahistidine (6×His)-tag removal was carried out by the addition of 1 mg His-tagged TEV protease and 1 mM dithiothreitol (DTT) and standing overnight at 4 °C. The residual amino acid sequences after the digestion are GHM. The reaction mixture was loaded onto the HisTrap HP column again, and the flow-through fraction was collected and diluted ten times with the dialysis buffer. The diluted solution was loaded onto a 1 ml Resource Q column (GE Healthcare), and the protein was eluted by a 30–750 mM NaCl gradient. The FtsZ fractions

were further purified using a HiLoad 16/600 Superdex 200 prep-grade column (GE Healthcare) equilibrated with gel-filtration buffer (20 mM Tris-HCl pH 7.5, 150 mM NaCl). The purity of the protein was confirmed by SDS-PAGE. The purified protein was concentrated to 10 mg ml^{-1} with Vivaspin 20-10K (GE Healthcare), and flash-frozen in liquid nitrogen and immediately stored at -80 °C. R29A mutant of SaFtsZ$_{12-316}$ was cloned, expressed, and purified as described above, except that site-directed mutagenesis was performed by inverse-PCR using the following primers: forward, 5'-CAACGCCGTAAACgcAATGATTGACC-3', reverse, 5'-GGTCAATCATTgcGTTTACGGCGTTG-3' (The changed nucleotides are represented in small letters, and the codons corresponding to the amino acids residues to be changed are underlined).

1.2.2. Crystallization, data collection and structure determination

All SaFtsZ crystals in this chapter were obtained by a sitting-drop vapor-diffusion technique at 20 °C in the following reservoir conditions based on JBScreen Pentaerythritol 2 (Jena Bioscience). SaFtsZ$_{12-316}$–GDP complex was crystallized at 4.4 mg ml^{-1} under the condition of 100 mM HEPES pH 8.0, 39% w/v pentaerythritol propoxylate 629 (PEP 629). SaFtsZ$_{12-316}$ R29A (T state) was crystallized at 10 mg ml^{-1} under the condition of 100 mM Tris pH 8.1, 43% w/v PEP 629, 300 mM KCl. SaFtsZ$_{12-316}$ R29A (R state) was crystallized at 10 mg ml^{-1} under the condition of 100 mM Tris pH 8.4, 45% w/v PEP 629, 300 mM KCl. Crystals were flash-frozen in a nitrogen gas stream at -180 °C without cryoprotectants. X-ray diffraction data were collected at SPring-8 BL44XU (Hyogo, Japan) under cryogenic nitrogen gas stream at 100 K. The diffraction data were processed and scaled with HKL2000 (54). The phases were determined by molecular replacement with Phaser in the CCP4 suite (55) using a previous structure of SaFtsZ–GDP complex (PDB entry: 3VOA) (23) as a search model. The model structures were refined with Refmac5 (56) and CNS (57, 58), with manual modification using COOT (59). The refined structures were validated with MolProbity (60). Data collection and refinement statistics are summarized in Table 1-1. The final atomic coordinates and structure factor amplitudes have been deposited in the RCSB Protein Data Bank (PDB entries: 5H5G, 5H5H, and 5H5I). Chain

interactions were assessed with PISA server (61), and interface interactions were identified with LIGPLOT (62). Domain rotation was estimated with DynDom (63). Sequence alignment was prepared using ClustalW (64) and ESPript (65). Figures were prepared with PyMOL (Schrödinger).

1.2.3. GTPase activity assay

GTPase assay of SaFtsZ was carried out using a coupled enzyme assay (66). In this method, GTP hydrolysis is coupled to NADH oxidation with pyruvate kinase (PK) and lactate dehydrogenase (LDH). NADH absorbance decrease at 340 nm was measured, which is proportional to the rate of GTP hydrolysis. In our experiments, the sequential reactions were performed in 50 mM Tris-HCl pH 7.5, 5 mM $MgCl_2$, 200 mM KCl, 50 U ml^{-1} PK, 50 U ml^{-1} LDH, 1 mM phosphoenolpyruvate (PEP), 1 mM GTP, 0.2 mM NADH, 0.5 mg ml^{-1} protein at 37 °C. Whole reaction volume was 1 ml. GTPase activity was calculated from the decrease of absorbance per minute at 340 nm divided by the molar extinction coefficient of NADH (6220 M^{-1} cm^{-1}), FtsZ molar concentration, and the path length (1 cm).

1.2.4. MD simulations

PaCS-MD and conventional MD simulations were performed by co-workers (67).

Table 1-1. Data collection and refinement statistics.

Data set	SaFtsZ$_{12-316}$ WT	SaFtsZ$_{12-316}$ R29A (T state)	SaFtsZ$_{12-316}$ R29A (R state)
PDB entry	5H5G	5H5H	5H5I
Data collection			
X-ray Source	SPring-8 BL44XU	SPring-8 BL44XU	SPring-8 BL44XU
Wavelength (Å)	0.900	0.900	0.900
Space group	$P2_1$	$C2$	$C2$
Unit-cell parameters			
a, b, c (Å)	43.92, 159.02, 44.06	71.53, 50.83, 88.48	64.76, 59.28, 81.77
β (°)	92.78	110.63	109.13
Resolution (Å)	50.0–2.20 (2.24–2.20)[1]	50.0–1.70 (1.73–1.70)	50.0–1.90 (1.93–1.90)
Total reflections	156,805	132,869	86,369
Unique reflections	30,358	32,530	22,985
Completeness (%)	100.0 (100.0)	99.5 (100.0)	99.2 (99.5)
I/σ	19.9 (2.2)	14.3 (1.4)	24.0 (2.0)
R_{merge}[2] (%)	8.0 (51.6)	13.0 (96.0)	6.4 (50.3)
$CC_{1/2}$ (%)	(80.0)	(87.1)	(84.3)
Refinement			
Resolution (Å)	44.0–2.20	41.4–1.70	42.6–1.90
R_{work}/R_{free}[3] (%)	18.4/24.5	18.2/22.6	18.9/22.3
No. of molecules in the A.U.	2 (T, R states)	1 (T state)	1 (R state)
No. of atoms			
Protein	4473	2230	2208
Ligand	57	29	28
Water	196	244	124
Average B-factors (Å^2)			
Protein (T state)	38.4	27.4	
Protein (R state)	47.2		43.2
Ligand	29.1	18.5	32.2
Water	42.1	34.9	44.4
RMSD from ideal			
Bond length (Å)	0.008	0.015	0.014
Bond angles (°)	1.359	1.707	1.695
Ramachandran plot			
Favored	608 (97.4%)	301 (97.1%)	300 (98.0%)
Allowed	16 (2.6%)	9 (2.9%)	6 (2.0%)
Outlier	0 (0%)	0 (0%)	0 (0%)

[1]Values in parentheses are for the highest resolution shells.

[2]$R_{merge} = \Sigma_{hkl} \, \Sigma_i \, |I_i(hkl) - <I(hkl)>|/\Sigma_{hkl} \, \Sigma_i \, I_i(hkl)$, where $I_i(hkl)$ is the intensity of an individual reflection and $<I(hkl)>$ is the mean intensity of symmetry-equivalent reflections.

[3]$R_{work} = \Sigma_{hkl} \, ||F_{obs}| - |F_{calc}||/\Sigma_{hkl} \, |F_{obs}|$, where F_{obs} and F_{calc} are observed and calculated structure-factor amplitudes, respectively. R_{free} was calculated as for R_{work} but using only 5% unrefined subset of reflection data.

1.3. Results and Discussion

1.3.1. Structure comparison between the T and R states

The GTPase enzymatic domain (residues 12–316) of SaFtsZ was expressed, purified, and crystallized as described above. The crystal structure was determined at 2.2 Å resolution, and all SaFtsZ molecules in the crystal bound GDP, which did not be supplemented in the purification or crystallization steps. Therefore, it should be brought from *E. coli* during the cultivation. The crystallographic asymmetric unit contains two structurally different SaFtsZ molecules (chains A and B, a root mean square deviation (RMSD) = 1.2 Å for aligned 229 C_α atoms; Fig. 1-2A). Chain A shows the common structural features of most previously determined SaFtsZ structures (e.g. PDB entry 3VOA, RMSD = 0.20 Å for aligned 256 C_α atoms, Fig. 1-2B) (23), whereas the structure of chain B is similar to that of ΔT7 mutants of SaFtsZ (PDB entries 3WGK and 3WGL, RMSD = 0.52 Å for aligned 248 C_α atoms and 0.61 Å for aligned 243 C_α atoms, respectively) (24) or FtsZ from other species (e.g. BsFtsZ, PDB entry 2RHL, RMSD = 0.82 Å for aligned 234 C_α atoms, Fig. 1-2C) (68). Thus, it is concluded that the conformations of chain A and B correspond to those of the T and R states, respectively. This is the first example that both of the conformations were observed in non-mutated FtsZ from a single species. Although the N-terminal subdomains (residues 12–172) of the T and R state structures are well superposed (RMSD = 0.44 Å), the C-terminal subdomains (residues 222–316) are not (RMSD = 1.1 Å) because of approximately 23º (calculated by DynDom (63)) rotation of the C-terminal subdomain. Structure comparison of the T and R state also highlights significant structural differences in three areas: the GDP-binding site and the H7 helix, the intersubdomain region, and the T7 loop (Fig. 1-2A).

Superposed on the phosphate and the ribose moiety of GDP, the guanine ring is tilted approximately 30º, and the H7 helix moves upward in the R state relative to the T state (Fig. 1-3A, B). In the T state, Arg29 is hydrogen-bonded with the carbonyl group of the guanine ring and Asp187, but the side chain of Arg29 is flipped outside in the R state and Asp187 binds to the guanine ring directly. Note that the equivalent Arg-Asp ion pairs between the H1 and H7 helices are highly conserved in many bacterial species (69). His33 in the H1 helix forms NH-π or cation-π interaction with Arg191 both in
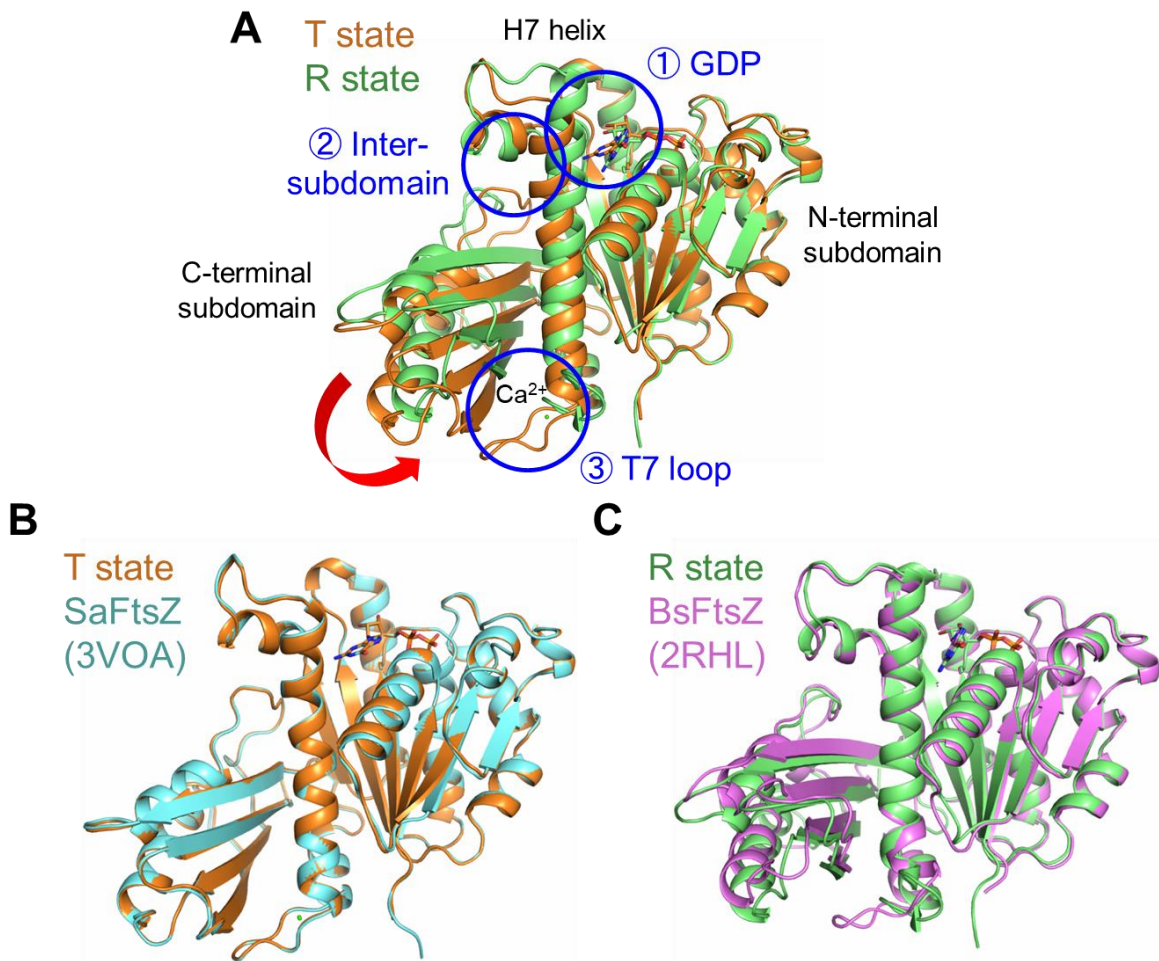
Figure 1-2. Whole structure comparison of FtsZ. (A) Superposition of the T (orange) and R (green) state in this study. Three areas where significant structural changes were observed are highlighted by blue circles. The rotation of the C-terminal subdomain is indicated by a red curved arrow. (B) Superposition of the SaFtsZ in this study (orange) and the previous one (cyan, PDB entry: 3VOA) in the T state. (C) Superposition of the SaFtsZ in this study (green) and BsFtsZ (purple, PDB entry: 2RHL) in the R state.

the T and R state, and fixes the position of Arg191.

In the region between the N- and C-terminal subdomain, there are two pairs of hydrogen bonds in the T state: the side chains of Arg134 and Glu251, and the main chains of Val163 and Glu251 (Fig. 1-3C). In the R state, however, neither hydrogen bond is observed (Fig. 1-3D). This might be related to the interaction change that Asn166 binds to the GDP directly in the T state but Thr133 forms a water-mediated hydrogen bond to the GDP in the R state. The loss of the hydrogen bonds results in a structural change of the H9–S8 loop (residues 245–258) and probably the C-terminal subdomain rotation.

15

In the T7 loop of the T state, four residues (Leu200, Val203, Asn208, and Leu209) and two water molecules are octahedrally coordinated to the Ca^{2+} ion (Fig. 1-3E). The Ca^{2+} coordination sphere is essentially the same as in the previous structure (23) and assures the T7 loop rigidity, enabling it to be deeply inserted into the nucleotide-binding pocket of the neighboring molecule. The residues in the edge of the T7 loop also binds the residues located on the S9 strand to keep the binding cleft for the FtsZ inhibitor PC190723 (PC cleft) open (23, 46). In the R state, the T7 loop adopts significantly different conformation (Fig. 1-3F). The T7 loop structure in the R state does not contain Ca^{2+}, and four hydrogen bonds are formed between three pairs of residues (Leu200–Leu209, Ile201–Asn208 and Val203–Glu206), resulting in the formation of a twisted β-hairpin-like structure. Such a large movement of the T7 loop has not been observed in previous FtsZ crystal structures. The side chain of Asn208, which participates in Ca^{2+} capture in the T state, is hydrogen-bonded with the carbonyl group of Thr296 in the S9 strand. Moreover, the carbonyl group of Gly196 in the H7 helix forms a hydrogen bond with the side chain of Asn263 located on a β-sheet in the C-terminal subdomain to close the PC cleft in the R state. Switching between these interactions coordinates the open or closed motions of the PC cleft. Furthermore, the Gly196–Asn263 interaction disrupts the terminal structure of the H7 helix, supporting the reorientation of the T7 loop. The structural basis of the SaFtsZ conformational changes observed here might be common to many bacterial species, because Gly196 and Asn208 are highly conserved among members of the FtsZ family.
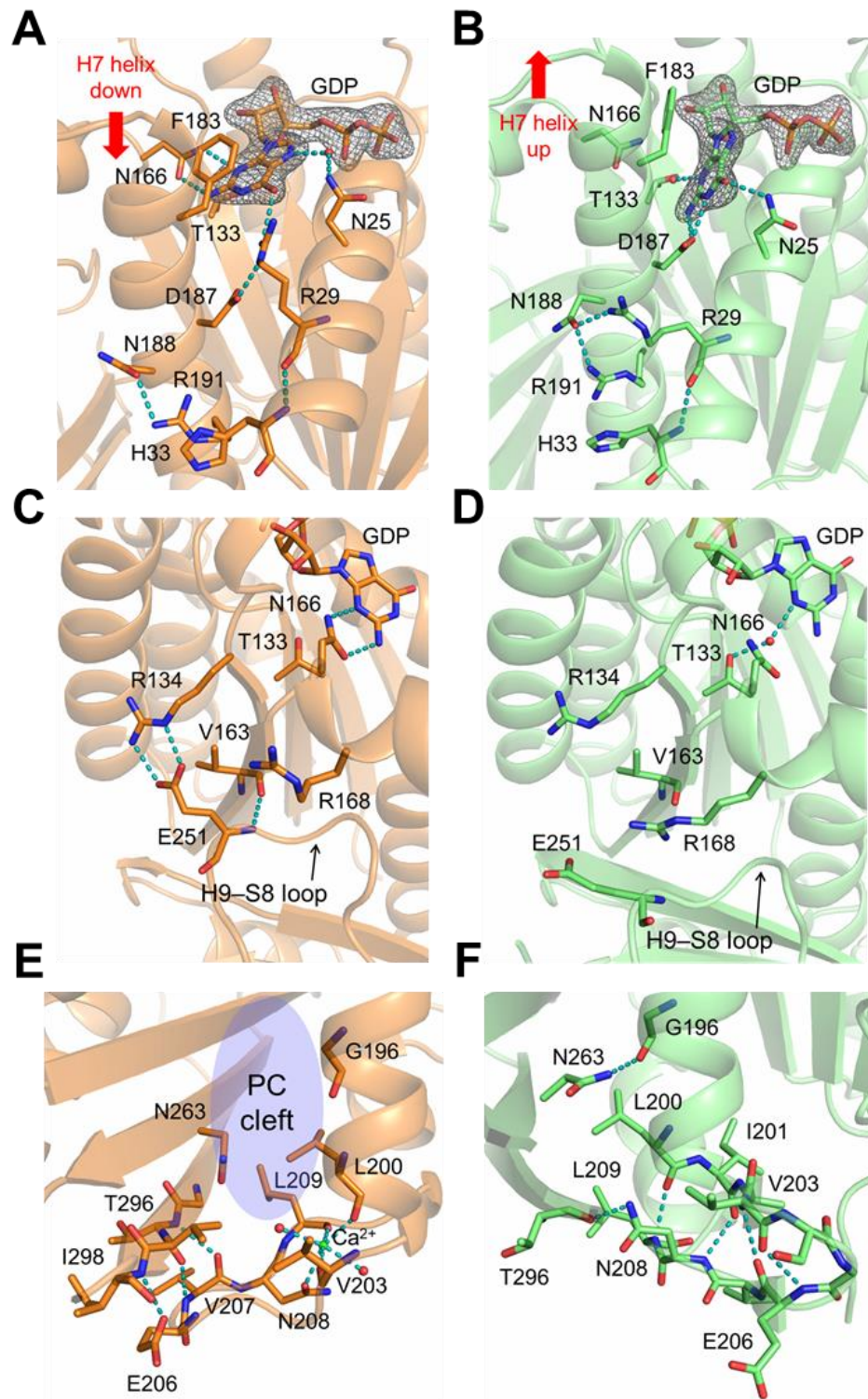
Figure 1-3. Structure comparison between the T and R states. (A, B) Interactions around the GDP, H1, and H7 helix in the T (A) and R (B) state. The mF_o–DF_c omit maps are contoured at 3.5 σ as gray meshes. Water molecules are shown by red spheres. Hydrogen bonds are shown by cyan dotted lines. (C, D) Interactions around the intersubdomain region in the T (C) and R (D) state. (E, F) Interactions around the T7 loop in the T (E) and R (F) state.

The structural changes in the FtsZ monomer also affect interactions with neighboring molecules in the filaments. In the crystal, two kinds of layers consisting of only either the T or R monomer are accumulated alternately, and the directions of FtsZ filaments in each layer are oriented perpendicularly (Fig. 1-4A). The repeat distances between monomers in the T and R filament are 44.1 Å and 43.9 Å, respectively. In the T filament, the interface can be divided into two parts: the left and the right one (Fig. 1-4B). The left one contains the hydrogen bond between Leu270 (main chain CO) and Met179 (main chain NH) in the H6–H7 loop of the lower molecule. The corresponding interaction is maintained in the R state, although the interaction pair is changed into Leu272 (main chain NH) and Thr177 (main chain CO) (Fig. 1-4C). Because Thr177 and Met179 are located near the N-terminus of the H7 helix, this interaction change may lead to an up/down shift of the helix. In the right-side interaction, the T7 loop is deeply inserted into the GTP/GDP binding pocket of the neighboring molecule in the T state as the previous structure (23). The main chain carbonyl group of Glu206 in the T7 loop forms a hydrogen bond with the side chain of Asn25 in the H1 helix of the lower molecule (Fig. 1-4B). Notably, Asn25 is also highly conserved among bacterial species. In contrast, this interaction is not observed in the R state because of the flipped T7 loop (Fig. 1-4C). As a result, the interaction areas decrease from 1168 $Å^2$ in the T state to 798 $Å^2$ in the R states. Such reduction in surface area in the R state interface results in a gap on one side of the protofilament, which might permit bending, as reported previously (24, 25). The relative orientation of the neighboring molecules in the filament differs between the T and R state structures (Fig. 1-4D). Superposed on the upper molecules of the T and R filament, the lower molecule shifts about 8 Å, resulting in reorientation between neighboring molecules in the filaments.

Based on the crystal structures, the T–R structural change mechanism could be proposed as follows (Fig. 1-5): after GTP hydrolysis, first, tilt of the guanine ring and interaction changes around the GDP are occurred. This also causes the dissociation of the hydrogen bonds between N- and C-terminal subdomains. The loss of the hydrogen bonds leads to the rotation of C-terminal subdomain and upshift of the H7 helix. Then the T7 loop is pulled out from the GTP/GDP binding pocket of the neighboring molecule and flipped out to reduce the interaction area, which promotes reorientation of the neighboring

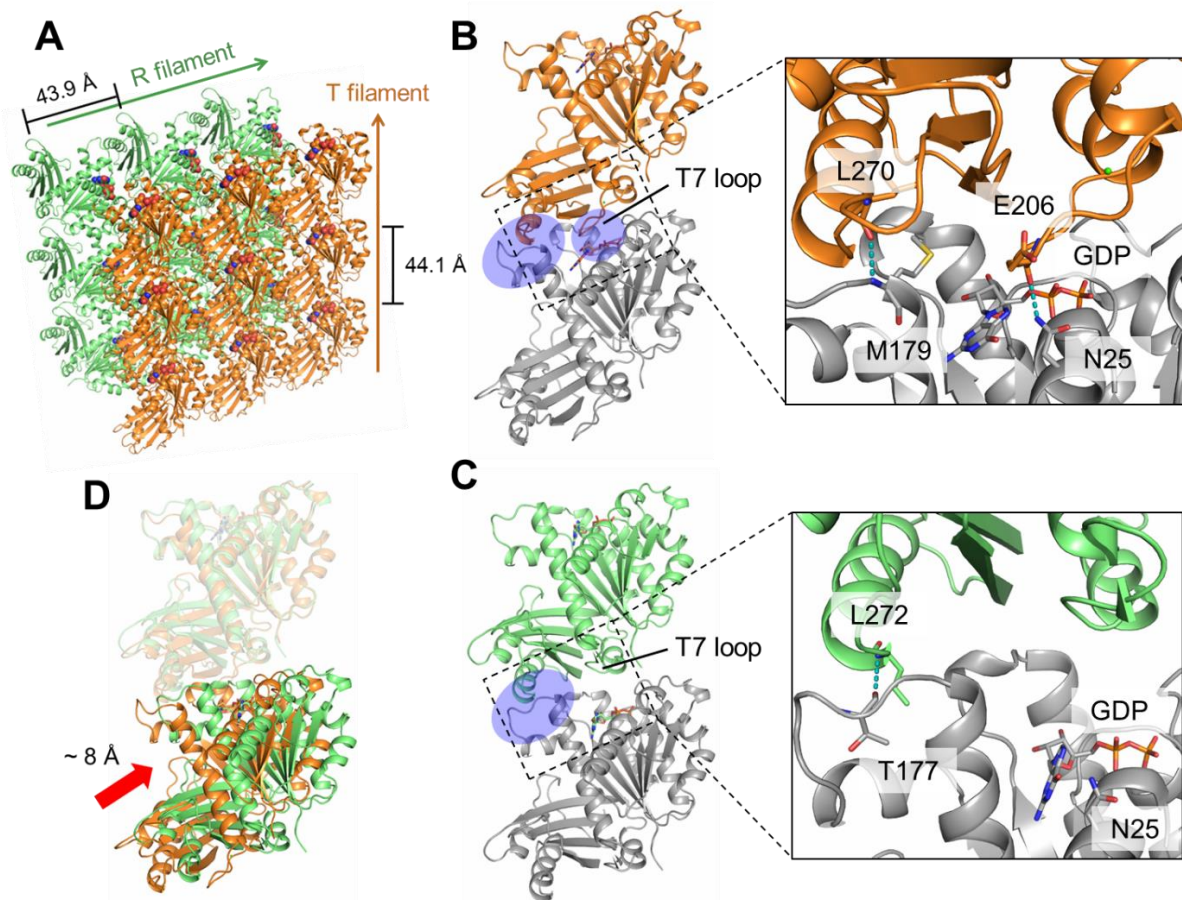molecule to allow the curvature of FtsZ protofilaments.

Figure 1-4. Intermolecular interactions of SaFtsZ. (A) Crystal packing and filaments arrangement. Molecules in the T and R state are shown in orange and green, respectively. (B, C) Dimer structures of the T (B) and R (C) filament (left panel). Lower molecules are colored in gray. Interaction areas are highlighted by blue circles. Close-up views of the interaction areas (right panel). Hydrogen bonds are shown by cyan dotted lines. (D) Superposition of (B) and (C) left panel based on the upper molecules (shown in semi-transparent). Movement between the lower molecules is indicated by a red arrow.
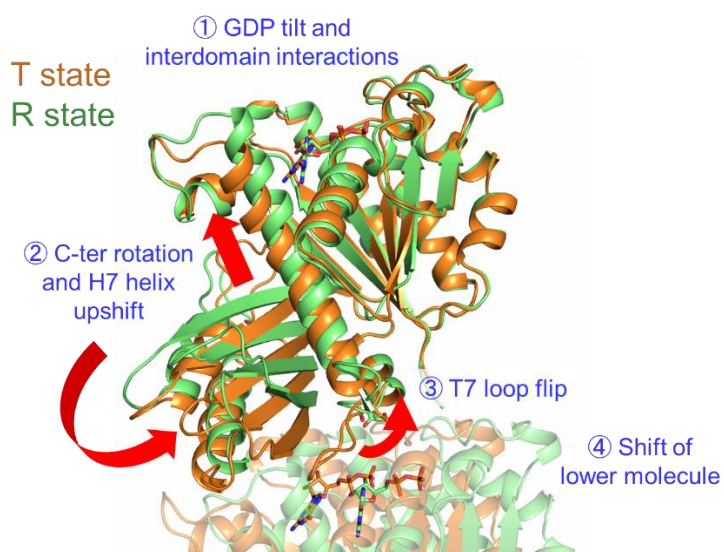

Figure 1-5. Proposed mechanism of T–R structural change. Significant movements are indicated by red arrows.

1.3.2. Transient structure and key interactions identified by PaCS-MD

In order to verify and investigate the proposed mechanism of the T–R structural change, PaCS-MD simulations (67) followed by free-energy analyses were applied to each monomer in the T and R states in this study by co-workers. After 300 cycles (total 300 ns), the simulation successfully reproduced the structural change to near the crystal structure of the R state (RMSD = 1.2 Å for aligned 260 C_α atoms, Fig. 1-6A), similar to the previous MD simulation (28). Nevertheless, neither of them reproduced the flip of the T7 loop. In addition, this T7 reorientation was not reproduced in the extra PaCS-MD simulations without Ca^{2+}. This is probably because intermolecular interaction is needed for the T7 loop reorientation. A free-energy profile during the T–R structural change clearly suggests the existence of a transient structure between the two stable T and R states in aqueous solution (Fig. 1-6B). The low energy barrier (about 4 k_BT) indicates that the structural change easily occurs at room temperature, and both T and R states co-exist in solution. The free energy difference between the T and R states is about one k_BT. Roughly speaking, this free energy difference corresponds to the existence ratio of the T state (0.55) : R state (0.45) in the equilibrium, although the free energy profile is strongly affected by a choice of force field parameters in MD simulations. In this transient structure snapshot, the C-terminal subdomain and the H7 helix are located between those of the T and R state (Fig. 1-6C).

Focused on the interactions around GDP in this transient structure (Fig. 1-6D, middle panel), the following features were found from the comparison to those in the T and R state (Fig. 1-6D, left and right panel, respectively). (1) GDP interacts with Arg29 in the T state and is directly bound to Asp187 in the R state. On the other hand, Asp187 is hydrogen-bonded with both GDP and Arg29 in the transient structure. (2) Asn166 forms hydrogen bond with GDP in the T state, but Thr133 interacts with GDP through a water-mediated and direct hydrogen bond in the R state and transient structure, respectively. (3) π-π stacking between Phe183 and the guanine ring of GDP is observed in both T and R state structures, whereas it is dissociated in the transient structure. These features suggest that this snapshot reasonably represents the transient structure between the T and R state well. Additionally, in the transient structure, the unique hydrogen bond was also found between the side chains of Arg191 and

the main chain carbonyl oxygen of Arg29, which is absent both in the T and R state crystal structure. For further investigation, the distances between several hydrogen bonds were monitored during PaCS-MD simulations (Fig. 1-6E). A sudden dissociation of the hydrogen bond between Asn166 and GDP found in the T state was observed (green line at 900 ps), which suggests that this hydrogen bond was broken in the early stage of the structural change from the T to R state. Arg29 gradually approaches Arg191 to form a hydrogen bond formation between them (red line from 800 to 1000 ps). Owing to the hydrogen bond formation between Arg191 and Arg29, Arg29–GDP interaction was weakened and Asp187 was inserted between them as the transient structure, resulting in the dissociation of Arg29 from the GDP (blue line at 1080 ps). Finally, the Arg29–Arg191 hydrogen bond was broken to complete the structural changes to the R state structure (red line at 1150 ps). Among FtsZ proteins, Asn166 and Thr133 are completely conserved, and Arg29 and Asp187 are well conserved, but His33, Asn188, and Arg191 are not. This tendency may indicate that the switching residues related to the T–R change are well conserved, but the interaction pairs of the switching residues differ among bacterial species.

In this study, the PaCS-MD simulation was applied only for monomer structure, but both intramolecular and intermolecular changes have to be cooperative (70). Additionally, the GTP/GDP exchange also affects FtsZ conformation, because the presence of a γ-phosphate and its interaction with the T3 loop would strongly affect the conformation of the neighboring molecule in other species (25). However, this structural change has not been observed in SaFtsZ (24). Further MD studies of FtsZ filament based on a crystal structure of the complex of SaFtsZ and GTP (or its analog) at higher resolution than the previous one (24) may be considered to address the complete T–R structural change.
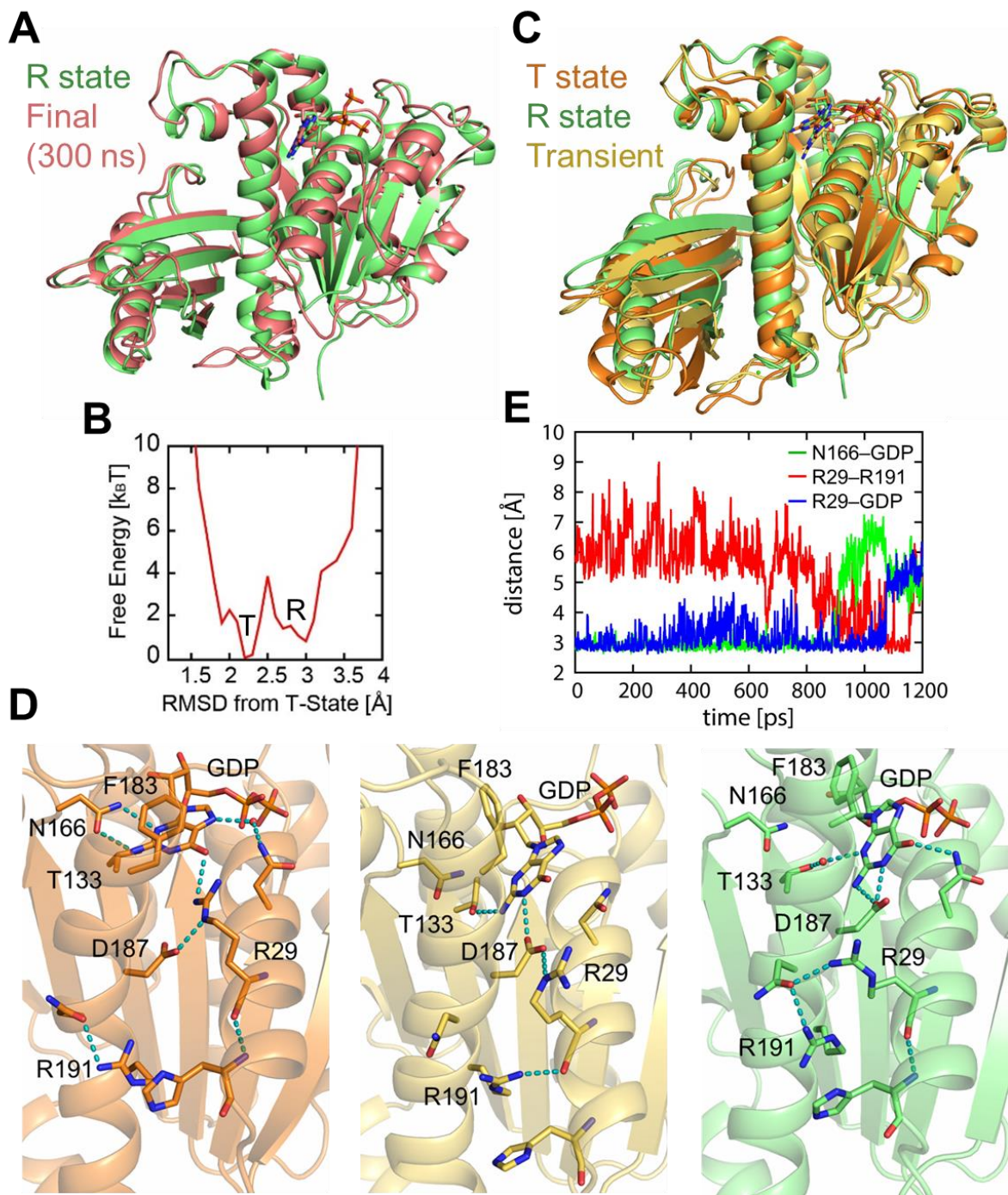
21

Figure 1-6. PaCS-MD simulation for T–R structural change. (A) Superposition of crystal structure of the R state (green) and final structure after 300 ns calculation (red). (B) Profile of free energy calculation as a function of C_α RMSD measured from crystal structure of the T state in this study. (C) Superposition of the T (orange), R (green), and the transient structure (yellow). (D) Interactions around GDP in the T state (left), transient structure (middle), and the R state (right). Hydrogen bonds are shown by cyan dotted lines. (E) Profile of hydrogen bond distances during the T–R structural change between Asn166–GDP (green), Arg29–Arg191 (red), and Arg29–GDP (blue).

1.3.3. Crystal structures and conventional MD simulations of R29A mutant in the T and R state

To confirm the importance of the residues in the T–R structural change, we focused on Arg29, which moved markedly in the T and R crystal structures and the calculated transient structure, and is well conserved among many bacterial species. The mutant that Arg29 was replaced with Ala (R29A) was designed and prepared in the same way as WT. It was considered that R29A mutant adopted only the R state conformation, because the dissociation of Arg29–GDP hydrogen bond would destabilize the T state structure. As expected, R29A mutant was found to lack GTPase activity (Table 1-2), probably because polymerization is severely inhibited by the destabilization of the T state. However, this result does not correspond to the previous one. In FtsZ from *Methanococcus jannaschii*, R55A mutant (corresponds to R29A in SaFtsZ) shows a slightly higher GTPase activity than WT (69). This difference may be derived from the environment of surrounding residues. Although Arg55 and Asp212 (corresponds to Asp187 in SaFtsZ) are conserved, surrounding Glu59, Glu213, and Ile216 (corresponds to His33, Asn188, and Arg191 in SaFtsZ, respectively) are completely changed.

To evaluate mutational effects on the structure, the R29A crystal structure was determined. Four of five crystals contain only the R state (the best resolution is 1.9 Å), but surprisingly, one crystal shows the T state structure (1.7 Å resolution). Each space group is C2, and each asymmetric unit contains one FtsZ molecule. Although the R29A structure in the T state is superposed well on that of WT in the T state (RMSD = 0.27 Å for aligned 250 C_α atoms, Fig. 1-7A, left panel), the structure of the H1 helix C-terminus is slightly loosened. The hydrogen bond distances between Arg/Ala29 (CO)–His33 (NH) and Met30 (CO)–Gly34 (NH) are changed from 2.9 (WT) to 3.4 Å (R29A) (Fig. 1-7A, right panels). The R29A structure in the R state also resembles that of WT in the R state (RMSD = 0.72 Å for aligned 273 C_α atoms, Fig. 1-7B), but again is slightly different. The C-terminal subdomain is not rotated completely relative to its position in WT in the R state. As described above, the WT structure in the T state contains the two pairs of hydrogen-bonds, Arg134–Glu251 and Val163–Glu251, between the N- and C-terminal subdomains (Fig. 1-3C), and the R29A structure in the T state does. However, neither of these hydrogen bond pairs is present in the WT structure in the R state (Fig. 1-3D). Interestingly, only a single hydrogen
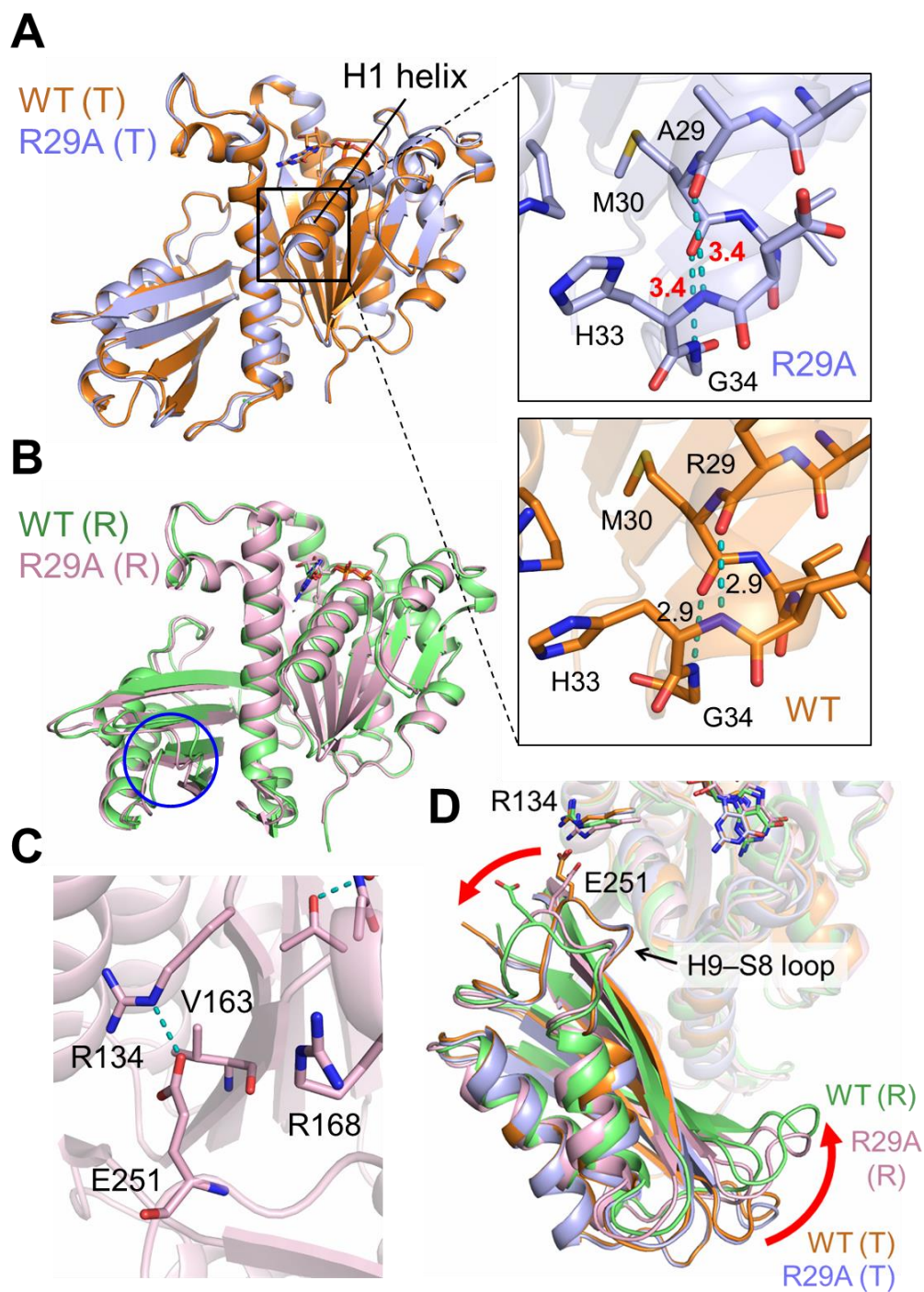
Figure 1-7. Crystal structures of R29A mutant in the T and R state. (A) Superposition of the WT (orange) and R29A (lightblue) in the T state (left panel). Close-up views around the H1 helix of the R29A (upper) and WT (lower) structures (right panel). Hydrogen bonds are shown by cyan dotted lines. The distances are labeled in Å. (B) Superposition of the WT (green) and R29A (pink) in the R state. Incomplete C-terminal subdomain rotation is highlighted by a blue circle. (C) Interdomain interactions of the R29A structure in the R state. (D) Superposition of the C-terminal subdomains of WT T (orange) and R (green) state, and R29A T (lightblue) and R (pink) state. The rotation directions are indicated by red arrows.

bond pair, Arg134–Glu251, is present in the R29A structure in the R state (Fig. 1-7C). Therefore, a degree of intersubdomain hydrogen bond dissociation correlates with that of the rotation of the C-terminal subdomain (Fig. 1-7D). The interactions between neighboring molecules were almost conserved between the mutant and WT.

Table 1-2. GTPase activity of SaFtsZ$_{12–316}$ WT and R29A mutant.

	GTPase activity (min^{-1})
WT	1.0 ± 0.06
R29A	$(8.5 \pm 0.9) \times 10^{-3}$

Average and standard error of three independent experiments are shown.

To address the effects of the mutation (R29A) on the T–R structural change, four conventional MD simulations were independently applied for the monomer structures of the WT and R29A mutant in the T and R state. After 100 ns of the simulations, C$_\alpha$ RMSDs measured from the T and R states of the WT crystal structures were calculated for all the snapshots. Then, these values were plotted as a two-dimensional distribution (Fig. 1-8). The distributions of the T (Green) and R (Red) states in the WT simulations were clearly separated from each other. On the other hand, those in the R29A mutant simulations partly overlapped, suggesting that both of the T and R states of the R29A structures are in between those of the WT and that the structures of R29A is more flexible in a solution due to the loss of Arg29–GDP hydrogen bond. From these results, the significance of Arg29 is confirmed as the conformational switch in the T–R structural change process.
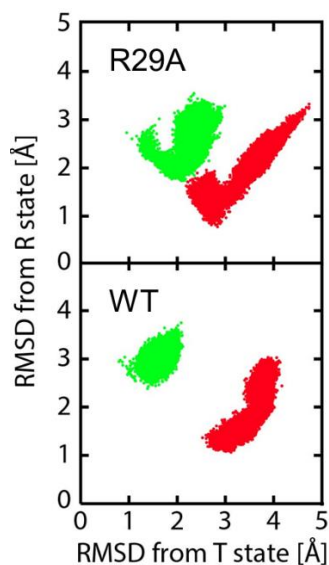
Figure 1-8. Projections of trajectories generated by conventional MD simulations (100 ns) starting from the T (green) and R (red) states of R29A mutant (upper panel) and WT (lower panel). Each trajectory was projected onto the conformational subspace spanned by a set of C_α RMSDs measured from the T and R states of WT.

1.4. Summary

In this chapter, the author reported the 3D structures of non-mutated SaFtsZ corresponding to the T and R state conformations in the same crystal for the first time and proposed the T–R structural change mechanism. PaCS-MD simulation performed by the co-workers enables us to predict the transient structure and identify key interactions during the conformational change. Crystallographic analysis and conventional MD simulations using the mutant also supported these results, which offers structural insights into the mechanism of T–R conformational change leading to the assembly/disassembly and the treadmilling of FtsZ molecules.

Chapter 2

Unique Binding Mode of FtsZ Inhibitors and

Relationship to Drug-Resistant Mutation

2.1. Introduction

As described in section 0.3, the benzamide derivative PC190723 has been shown to be efficacious inhibitor against MRSA. However, the poor pharmaceutical and pharmacokinetic characteristics has hampered its clinical use. Recently, my collaborators in the group of Professor Daniel S. Pilch at Rutgers Robert Wood Johnson Medical School, described a novel small molecule (TXA707) that targets SaFtsZ (71, 72). The chlorine substituent of PC190723 is replaced with a trifluoromethyl (CF_3) group for increasing stability against metabolic attack (Fig. 2-1). TXA707 is bactericidal against clinical isolates of *S. aureus* that are resistant to various important antibiotics, including MRSA, vancomycin-resistant *S. aureus* (VRSA), linezolid-resistant *S. aureus* (LRSA), and daptomycin-resistant *S. aureus* (DRSA). In addition, the collaborators have shown that a prodrug of TXA707 (TXA709), for improving its poor oral bioavailability, is also efficacious *in vivo* in mouse models of both systemic and tissue (thigh) infections with MRSA, which further highlights the potential clinical usefulness of FtsZ-targeting agents.

The collaborators also identified several SaFtsZ mutations (G196S, N263K, G193D, G196C, and G196A) that confer resistance to TXA707 as well as PC190723 by frequency of resistance (FOR) assay (72). G196S shows the highest FOR (55%), while the others indicates much lower FOR values (less than 15%). This tendency is in a great accordance with the previous result using PC190723 (46). Actually, the result of minimal inhibitory concentration (MIC) assay against the MRSA clinical isolate MPW020 indicates that TXA707 is inactive against G196S mutant strain (>64 μg ml^{-1}) although it shows comparable activity (1 μg ml^{-1}) in WT FtsZ strain to that of PC190723 (Table 2-1) (73). The collaborators also found that the benzamide derivative TXA6101 retains antistaphylococcal activity

against MRSA that expresses G196S mutant of FtsZ (MIC of 1 µg ml^{-1}). Additionally, TXA6101 is 8-fold more active (MIC of 0.125 µg ml^{-1}) than TXA707 in WT FtsZ strain. This compound was first reported by another group as part of a broad structure-activity relationship (SAR) study of antistaphylococcal FtsZ inhibitors (74, 75). The difluoro-benzamide portion of TXA6101 is identical to that of TXA707, but in TXA6101, the bromine-substituted oxazole and CF$_3$-substituted phenyl rings are linked by a single bond in contrast to the fused ring of TXA707 (Fig. 2-1). Moreover, the structure of TXA6101 was further extended to a new compound called TXD1107 with a reduced propensity for aggregation. The only chemical difference of TXD1107 is an addition of a methyl group in the linker region between the difluorobenzamide and oxazole moiety, and TXD1107 shows the same MIC values as that of TXA6101 both in WT and G196S strain (Table 2-1). The collaborators also evaluated the MIC of a compound called TXD1122, which lacks the bromo group of TXA6101. Interestingly, TXD1122 was found to be far less active (4 µg ml^{-1}) than TXA6101 in WT strain (Table 2-1); thus, the bromo functionality is a critical determinant of the enhanced antistaphylococcal potency in these FtsZ inhibitors.
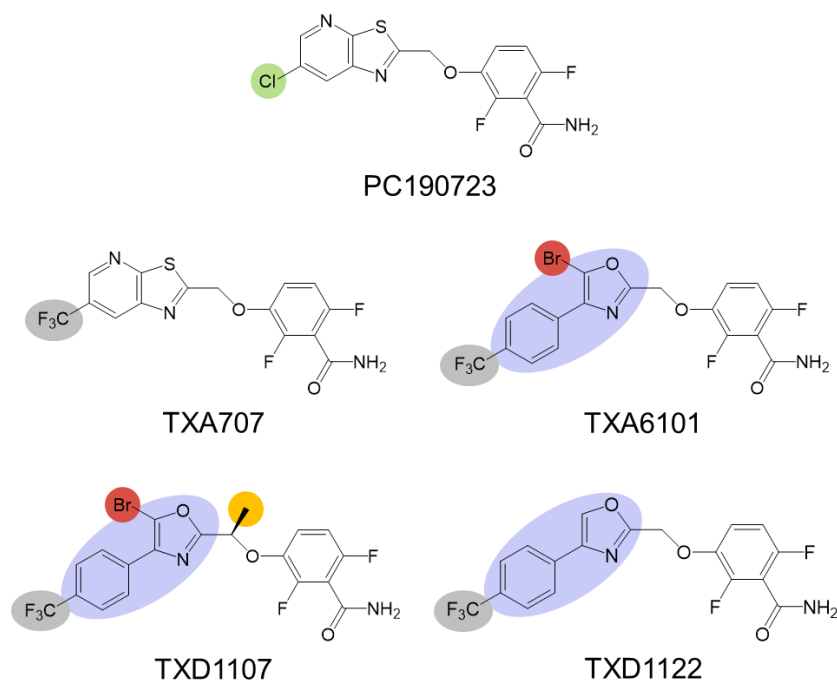

Figure 2-1. Chemical structures of the FtsZ inhibitors. The characteristic moieties are highlighted in each color.

Table 2-1. Activities of FtsZ inhibitors against MRSA MPW020 clinical isolates expressing FtsZ WT and G196S mutant.

compound	MIC (μg ml^{-1})	
	WT	G196S
PC190723	1[†]	>64[†]
TXA707	1	>64
TXA6101	0.125	1
TXD1107	0.125	1
TXD1122	4	ND

[†]Values against MRSA COL strain (46). ND denotes not determined.

Here, the author aims to investigate the binding manners of the newly developed inhibitors and the reason why TXA707 and TXA6101 (or TXD1107) show completely different activity against MRSA expressing G196S mutant. The author determined the crystal structures of TXA707, TXA6101, and TXD1107 in complex with WT SaFtsZ at the maximum resolution of 1.3 Å, the highest resolution among FtsZ to date, and found that these inhibitors bind FtsZ in a novel bent conformation. The structures explain the importance of bromo group of TXA6101 and TXD1107. The author also reported the crystal structures of SaFtsZ G196S in an inhibitor-free form and in complex with TXA6101. These structures demonstrate how the structural difference between TXA707 and TXA6101 affects the ability to target the G196S mutant.

2.2. Materials and Methods

2.2.1. Cloning, expression, and purification of SaFtsZ G196S mutant

SaFtsZ$_{12-316}$ was cloned, expressed, and purified as described in section 1.2.1. G196S mutant of SaFtsZ$_{12-316}$ was prepared in the same method, except that site-directed mutagenesis was performed by inverse-PCR using the following primers: forward, 5'-CCAAGGTGTACAAaGTATCTCAGACTTAATCG-3', reverse, 5'-CGATTAAGTCTGAGATACtTTGTACACCTTGG-3' (The changed nucleotides are represented in small letters, and the codons corresponding to the amino acids residues to be changed are underlined).

2.2.2. Crystallization, data collection and structure determination

The SaFtsZ crystals in this study were obtained using the sitting-drop vapor-diffusion technique at 20 °C in reservoir conditions based on JBScreen pentaerythritol 2 (Jena Bioscience). All SaFtsZ$_{12-316}$–inhibitor complexes were crystallized using a soaking method. For the complex of TXA707 with WT SaFtsZ, the protein was crystallized at 9.4 mg ml^{-1} under the condition of 100 mM Tris-HCl pH 7.6, 41% (w/v) PEP629, and 300 mM KCl. After 2 months, the crystal was soaked in the same reservoir supplemented with 5 mM TXA707 and 10% (v/v) 1-methyl-2-pyrrolidone for 2 days. For the complex of TXA6101 with WT SaFtsZ, the protein was crystallized at 9.4 mg ml^{-1} under the condition of 100 mM Tris-HCl pH 7.8, 43% (w/v) PEP629, and 300 mM KCl. After 3 weeks, the crystal was soaked in the same reservoir supplemented with 2 mM TXA6101 and 2% (v/v) dimethyl sulfoxide (DMSO) for 1 day. For the complex of TXD1107 with WT SaFtsZ, the protein was crystallized at 9.5 mg ml^{-1} under the condition of 100 mM Tris-HCl pH 7.8, 45% (w/v) PEP629, and 300 mM KCl. After 3 weeks, the crystal was soaked in the same reservoir supplemented with 5 mM TXD1107 and 10% (v/v) DMSO for 3 days. For the complex of TXA6101 with G196S mutant SaFtsZ, the protein was crystallized at 4.4 mg ml^{-1} under the condition of 100 mM Tris-HCl pH 8.4, 43% (w/v) PEP629, and 300 mM KCl. After 4 months, the crystal was soaked in the same reservoir supplemented with 5 mM TXA6101 and 10% (v/v) DMSO for 3 days. The inhibitor-free form of G196S mutant SaFtsZ was crystallized at 4.5 mg

ml^{-1} under the condition of 100 mM Tris-HCl pH 8.5, 45% (w/v) PEP629, and 300 mM KCl. Crystals were flash-frozen in a nitrogen gas stream at −180 °C without cryoprotectants. X-ray diffraction data were collected at SPring-8 BL44XU and BL32XU (Hyogo, Japan) under cryogenic nitrogen gas stream at 100 K. The diffraction data were processed and scaled with HKL2000 (54). The phases were determined by molecular replacement with Phaser in the CCP4 suite (55) using a previous structure of SaFtsZ–GDP complex (PDB entry: 3VOA) (23) as a search model. The model structures were refined with Refmac5 (56) and PHENIX (76), with manual modification using COOT (59). The refined structures were validated with MolProbity (60). Data collection and refinement statistics are summarized in Table 2-2. The final atomic coordinates and structure factor amplitudes have been deposited in the RCSB Protein Data Bank (PDB entries: 5XDT, 5XDU, 5XDV, and 5XDW) except SaFtsZ WT–TXD1107 complex for future publication. Interplanar angles were calculated using UCSF Chimera (77). Figures were prepared with PyMOL (Schrödinger).

Table 2-2. Data collection and refinement statistics.

Data set	WT–TXA707	WT–TXA6101	WT–TXD1107	G196S–TXA6101	G196S
PDB entry	5XDT	5XDU	not deposited	5XDV	5XDW
Data collection					
X-ray Source	SPring-8 BL44XU	SPring-8 BL32XU	SPring-8 BL44XU	SPring-8 BL44XU	SPring-8 BL44XU
Wavelength (Å)	0.900	1.100	0.900	0.900	0.900
Space group	$C2$	$C2$	$C2$	$C2$	$C2$
Unit-cell					
a, b, c (Å)	70.55, 51.19, 86.45	70.76, 51.57, 86.66	70.49, 51.74, 86.74	71.39, 50.44, 88.26	71.76, 51.01, 88.33
β (°)	108.68	108.75	108.65	109.97	110.71
Resolution (Å)	50.0–1.30 (1.32–1.30)[1]	50.0–2.00 (2.03–2.00)	50.0–1.40 (1.42–1.40)	50.0–1.70 (1.73–1.70)	50.0–2.00 (2.03–2.00)
Total reflections	503,253	55,580	360,570	121,237	110,946
Unique reflections	71,548	19,640	58,167	32,355	20,437
Completeness (%)	99.5 (100.0)	97.7 (98.3)	99.2 (100.0)	99.5 (100.0)	99.7 (99.8)
I/σ	41.7 (2.2)	13.6 (2.6)	26.7 (2.4)	27.7 (2.7)	17.6 (2.9)
R_{merge}[2] (%)	4.9 (76.0)	8.1 (26.4)	7.2 (70.4)	6.0 (36.8)	14.6 (87.9)
$CC_{1/2}$ (%)	(84.1)	(89.8)	(87.1)	(89.7)	(79.1)
Refinement					
Resolution (Å)	41.0–1.30	40.9–2.00	41.1–1.40	41.5–1.70	41.3–2.00
$R_{\mathrm{work}}/R_{\mathrm{free}}$[3] (%)	13.6/16.8	20.1/23.9	14.5/17.7	17.3/20.6	18.8/23.6
No. of molecules in the A.U.	1	1	1	1	1
No. of atoms					
Protein	2393	2211	2387	2230	2213
Ligand	69	58	59	58	29
Water	304	168	340	219	168
Average B-factors (Å^2)					
Protein	24.8	32.3	20.6	28.4	24.7
Ligand	23.8	29.9	14.6	22.9	16.7
Water	39.1	37.2	34.8	37.1	30.3
RMSD from ideal					
Bond length (Å)	0.011	0.012	0.007	0.012	0.010
Bond angles (°)	1.746	1.578	1.434	1.735	1.448
Ramachandran plot					
Favored	334 (98.2%)	294 (96.7%)	333 (97.9%)	303 (98.4%)	299 (98.4%)
Allowed	6 (1.8%)	10 (3.3%)	7 (2.1%)	5 (1.6%)	5 (1.6%)
Outlier	0 (0%)	0 (0%)	0 (0%)	0 (0%)	0 (0%)

[1]Values in parentheses are for the highest resolution shells.

[2]$R_{\mathrm{merge}} = \Sigma_{hkl} \Sigma_i |I_i(hkl) - \langle I(hkl)\rangle|/\Sigma_{hkl} \Sigma_i I_i(hkl)$, where $I_i(hkl)$ is the intensity of an individual reflection and $\langle I(hkl)\rangle$ is the mean intensity of symmetry-equivalent reflections.

[3]$R_{\mathrm{work}} = \Sigma_{hkl} ||F_{\mathrm{obs}}| - |F_{\mathrm{calc}}||/\Sigma_{hkl} |F_{\mathrm{obs}}|$, where F_{obs} and F_{calc} are observed and calculated structure-factor amplitudes, respectively. R_{free} was calculated as for R_{work} but using only 5% unrefined subset of reflection data.

2.3. Results and Discussion

2.3.1. Crystal structures of WT SaFtsZ complexed with TXA707, TXA6101, and TXD1107

The author determined the crystal structures of SaFtsZ enzymatic domain (residues 12–316) in complex with TXA707, TXA6101, and TXD1107 refined at 1.3, 2.0, and 1.4 Å resolution, respectively. The inhibitors were dissolved in 1-methyl-2-pyrrolidone or DMSO and introduced by soaking as described above. Although no nucleotides or divalent cations were added during the purification or crystallization steps, the crystal structure contains GDP and Ca^{2+} again. In the TXA707 structure, two molecules of the solvent (1-methyl-2-pyrrolidone) were observed in the crystal structure, one in an inner space between FtsZ and GDP and the other on the molecular interface between neighboring FtsZ molecules without altering FtsZ conformation and crystal packing. The overall structures of SaFtsZ when complexed the inhibitors are essentially the same as that of inhibitor-free form of SaFtsZ in the T state in this study (the maximum RMSD = 0.61 Å for the TXD1107 complex) and that of previously-reported PC190723-complexed SaFtsZ (PDB entries: 3VOB and 4DXD, the maximum RMSD = 0.45 Å between 3VOB and the TXD1107 complex) (23, 46). Difference Fourier omit maps clearly show that the inhibitors bind to the intersubdomain PC cleft, the same position as PC190723 (Fig. 2-2A–D). The interactions around the benzamide moiety of the three inhibitors and PC190723 are mostly conserved. The existence of the bromo group of TXD1107 was also confirmed by anomalous dispersion signal derived from Br K-absorption edge (0.920 Å, the wavelength of X-ray was 0.900 Å, Fig 2-2C, magenta mesh). The methyl group of TXD1107 shows no significant interaction with FtsZ. The binding manners of TXA6101 and TXD1107 are quite similar, so only higher-resolution TXD1107-complexed structure is described below.
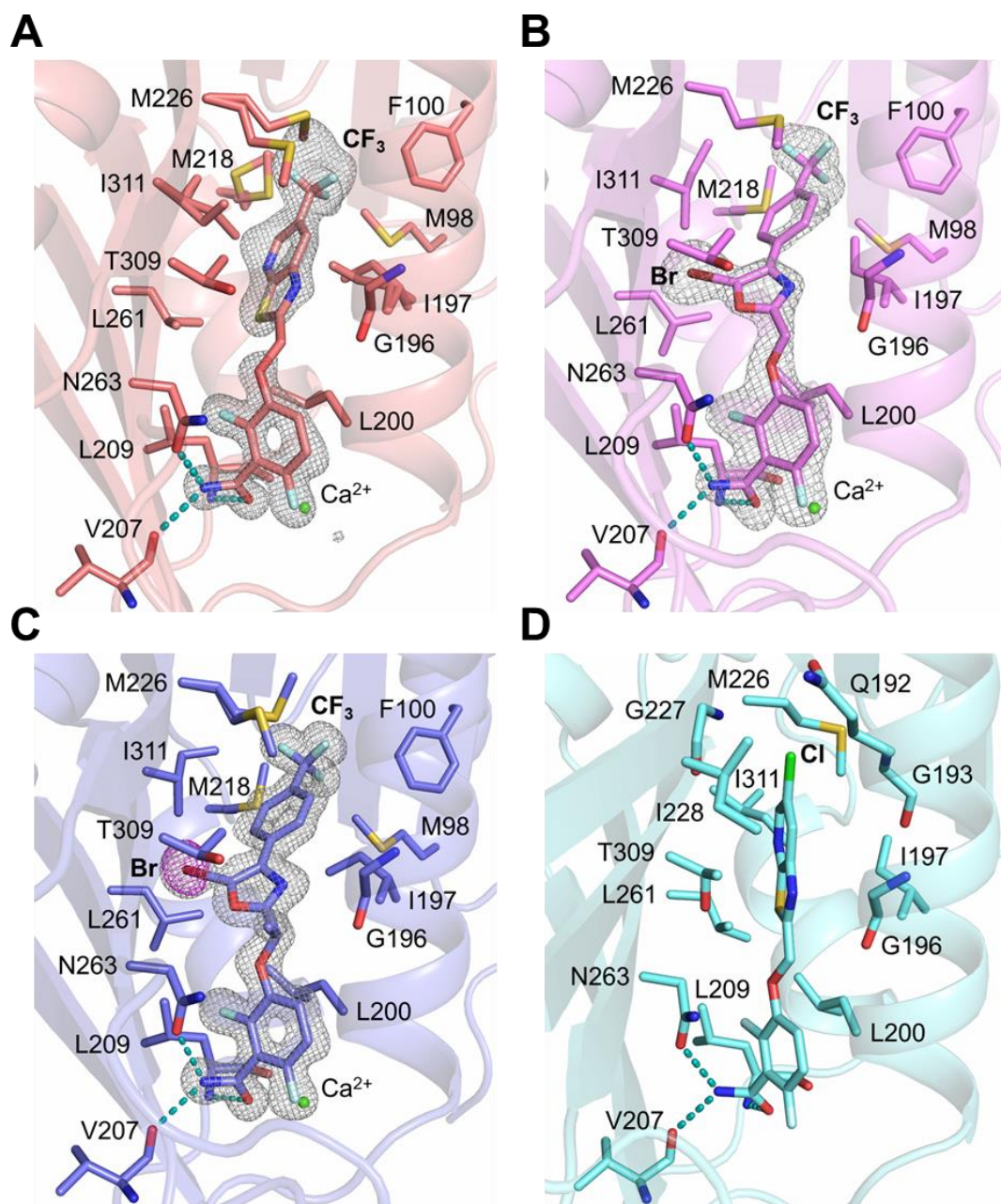
Figure 2-2. Close-up views of the inhibitor-binding sites in TXA707 (A), TXA6101 (B), TXD1107 (C), and PC190723 (D, PDB entry: 4DXD) complex. The mF_o–DF_c omit maps are contoured at 3.0 σ as gray meshes in (A), (B), and (C). Anomalous difference map is contoured at 5.0 σ as a magenta mesh in (C). Hydrogen bonds are shown by cyan dotted lines.

There is a significant conformational change in the inhibitors used in this study. All of TXA707, TXA6101, and TXD1107 adopt a novel "bent" conformation in contrast to the straight conformation of PC190723 (Fig. 2-3A). The CF_3-substituted rings of TXA707 and TXD1107 are accommodated in an inner hydrophobic pocket surrounded by the hydrophobic residues Met98, Phe100, Val129, Ile162, Gly193, Ile197, Val214, Met218, Met226, Leu261, and Ile311 (Fig. 2-3B, C). This pocket is unique to the novel inhibitor complexes, as it was not observed in previous structures of inhibitor-free SaFtsZ and SaFtsZ–PC190723 complex (23, 24, 46). In all previously-reported structures, the side chains of Ile197, Met226, and Ile311 block access to the inner hydrophobic pocket (Fig. 2-3D). Binding of TXA707 and TXD1107 induces conformational changes of the side chains of Ile197, Met226, and Ile311 to open the way to the hydrophobic pocket, which allows to accommodate the CF_3-substituted rings. The CF_3-substituted phenyl ring of TXD1107 is more extended than the corresponding CF_3-substituted thiazolopyridine ring of TXA707, and is therefore more deeply inserted into the inner hydrophobic pocket (Fig. 2-3A).

Superposition between the TXA707, TXD1107, and PC190723 complexes shows that the benzamide rings are precisely overlapped (Fig. 2-3A). Thus, the benzamide ring of TXA707 and TXD1107 is structurally stabilized via robust interactions within the binding cleft of FtsZ, and likely acts as a hinge point for the conformational changes of the other moiety in the compounds. The novel bent conformation and inner hydrophobic pocket we identified in this study provides the possibility of further structural optimization of the inhibitors. Within this hydrophobic pocket, extra space still remains around the CF_3 group of TXA707 and TXD1107 (Fig. 2-3B, C). The possibility of binding site extension along the intersubdomain cleft has recently suggested by MD simulation study using larger fluorescent analogs of PC190723 (78).
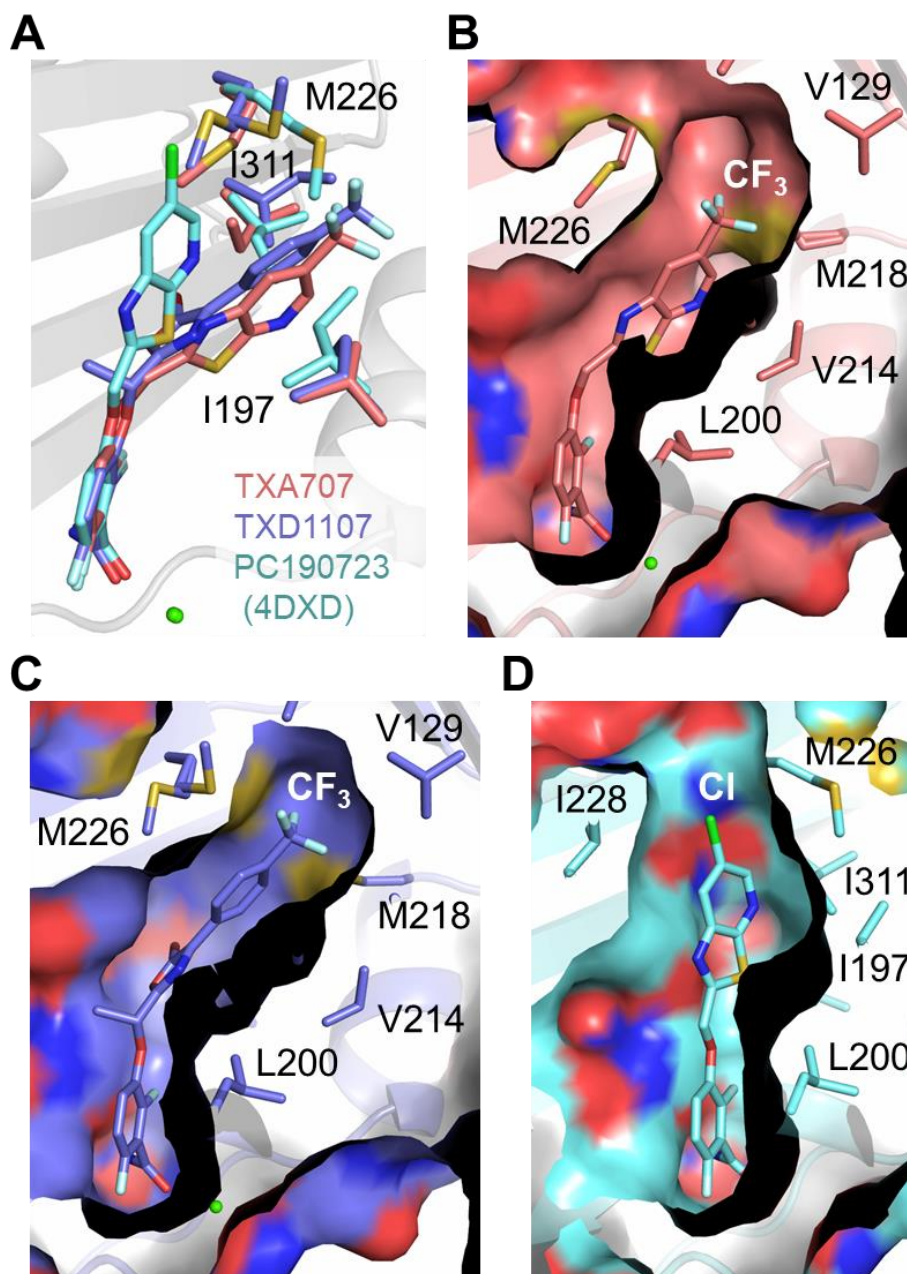
Figure 2-3. Different conformations of FtsZ inhibitors. (A) Superposition of the inhibitor conformations. The complex structures of TXA707, TXD1107, and PC190723 (PDB entry: 4DXD) are shown in pink, blue, and cyan, respectively. (B, C, D) Molecular surface of the binding pocket in TXA707 (B), TXD1107 (C), and PC190723 (D) complex.

The bent conformations of TXA707 and TXD1107 are also markedly different. The thiazolopyridine moiety of TXA707 is mainly stabilized by Van der Waals interactions with the side chains of Ile197, Leu200, Leu261, and Ile311 (Fig. 2-4A). During the initial refinement, positive differences in the Fourier map appeared in the residues surrounding TXA707, and the alternative

conformations of Ile197, Met226, and Ile311 were built into this density map. The minor conformers of Ile197, Met226, and Ile311 were very close to TXA707 (1.7–2.4 Å), suggesting they correspond to the conformations in the absence of the inhibitor. To minimize the positive difference peaks, the occupancy of TXA707 was set to 0.80, and those of Ile197, Met226, and Ile311 were set to 0.80 for the TXA707-bound form and 0.20 for the unbound form. This conformational alternation reflects the structural plasticity of the inhibitor binding pocket of SaFtsZ.

The bromo group on the oxazole ring of TXD1107 interacts with a hydrophobic pocket formed by the side chains of Leu261, Asn263, Thr309, and Ile311 located on the rigid β-sheet in the C-terminal subdomain of FtsZ (Fig. 2-4B). The distances between bromo group and the carbonyl oxygen of Leu261, the C_γ atom of Leu261, and the $C_{\gamma 2}$ atom of Ile311 are 3.1, 3.9, and 4.1 Å, respectively. These tight contacts offer the rigid orientation of the oxazole ring of TXD1107 in a conformation that is rotated approximately 55º relative to the corresponding thiazolopyridine rings of TXA707. Leu261 interacts with both TXA707 and TXD1107, but the way of interactions differs. One is with the sulfur atom on the thiazole ring of TXA707, and the other is with the bromo group on the oxazole ring of TXD1107. The interactions including the bromo group substantially contributes to the binding affinity with FtsZ, because the compound lacking this bromo group (TXD1122) shows 32-fold higher MIC value (Table 2-1). This robust bromo group interactions may also explain the result that the antistaphylococcal activity of TXD1107 and TXA6101 is 8-fold greater than that of TXA707.

The binding of TXA707 and TXD1107 induces conformational rearrangements of Ile197, Met226, and Ile311 that lead to open the way to the inner hydrophobic pocket. Here the question arises: why does the binding of TXA707 and TXD1107, but not PC190723, induce such conformational rearrangements in SaFtsZ to adopt the bent conformation? The only chemical difference between TXA707 and PC190723 is a substituent on the thiazolopyridine ring: CF_3 group for TXA707 and chloro group for PC190723. The previous PC190723–SaFtsZ complex structure enables us to predict the effect of replacing the chloro group in PC190723 with a CF_3 group. Such a substitution would introduce steric hindrances between the compound and residues Gln192, Gly193, and Gly227 (Fig. 2-2D). To avoid

37

such steric clashes, the movement of the side chain of Met226 leads to a series of conformational

rearrangements in residues Ile197 and Ile311. Conversely, if the CF_3 group of TXA707 was substituted

for the chloro group, sufficient interaction would not be formed in the inner hydrophobic pocket (Fig.

2-4C). Van der Waals radius of chlorine atom is 1.75 Å, and it is over 1 Å smaller than the size of CF_3

group of 2.78 Å (sum of the C-F distance of 1.31 Å in the TXA707 structure and Van der Waals radius

of fluorine atom of 1.47 Å).
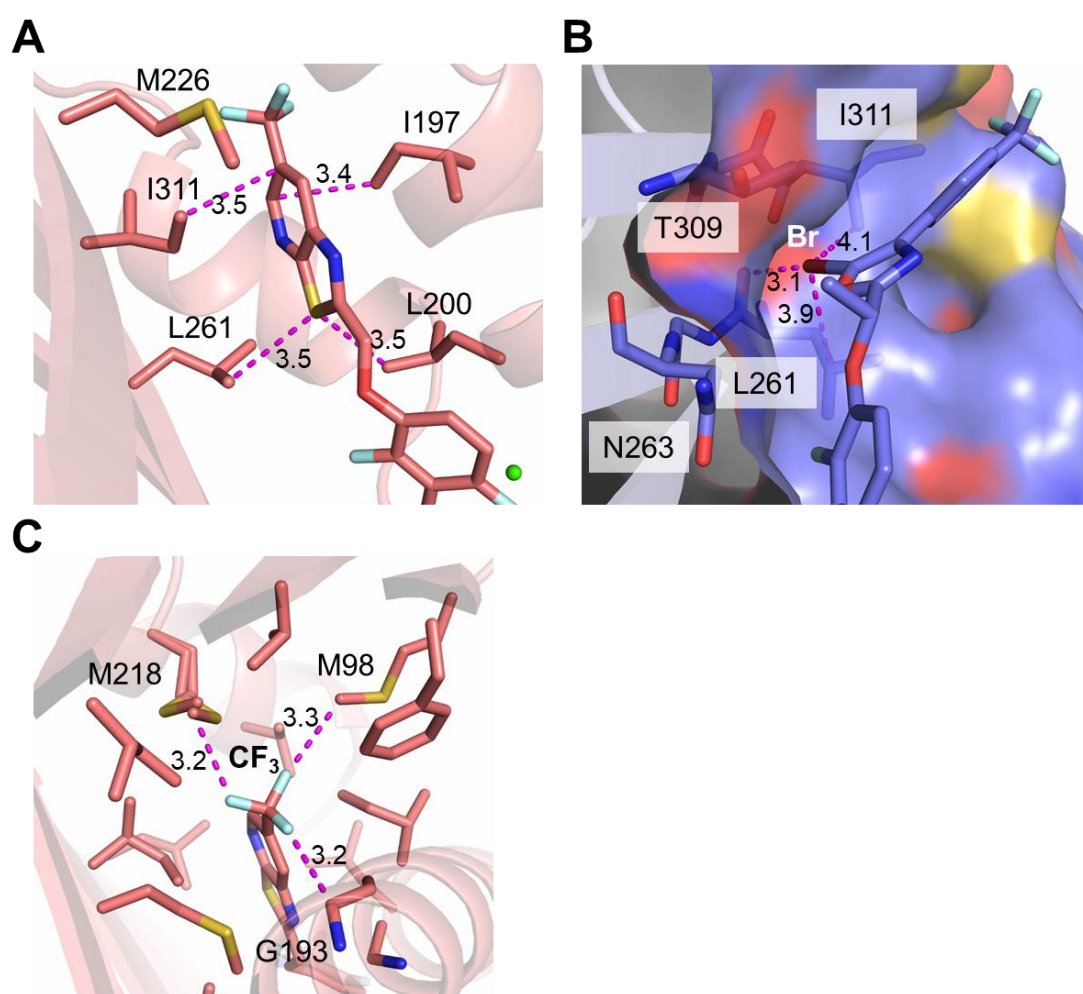
Figure 2-4. Different interactions between TXA707 and TXD1107. (A) Interactions around thiazolopyridine ring of TXA707. Van der Waals contacts are shown by magenta dotted lines. The distances are labeled in Å. (B) Interactions around bromo group of TXD1107. (C) Interactions around CF_3 group of TXA707 in the inner hydrophobic pocket.

2.3.2. Crystal structure of G196S mutant complexed with TXA6101

Next, the author determined crystal structures of SaFtsZ G196S–TXA6101 complex and inhibitor-free SaFtsZ G196S to investigate the reason why TXA6101 and TXD1107 retains activity against MRSA that expresses G196S mutant FtsZ, which remains resistant to TXA707 (Table 2-1). G196S–TXA6101 complex and G196S structures were refined at 1.7 and 2.0 Å resolution, respectively. The overall structures are essentially the same between G196S–TXA6101 complex and inhibitor-free G196S (RMSD = 0.49 Å for aligned 271 C_α atoms) and between inhibitor-free WT (T state in this study) and G196S structures (RMSD = 0.26 Å for aligned 279 C_α atoms) (Fig. 2-5A). These low RMSD values indicate that there are little structural effects of introducing G196S mutation and binding the inhibitor. In the G196S–TXA6101 complex structure, clear electron density corresponding to the inhibitor was observed in the same PC cleft as the previous inhibitor-complexed structures (Fig. 2-5B). The existence of the bromo group of TXA6101 was again confirmed by anomalous dispersion signal. The introduction of G196S mutation was also verified by the electron density in both structures, but the orientation of Ser196 side chain is completely reversed due to the steric hindrance with TXA6101.
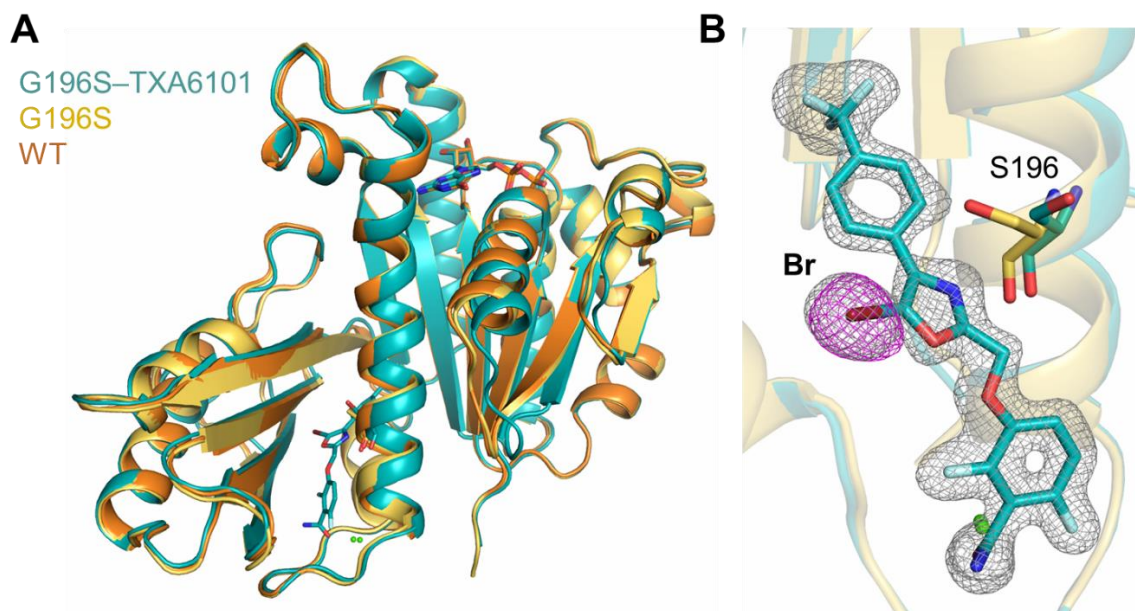
Figure 2-5. Crystal structures of G196S–TXA6101 complex and inhibitor-free G196S. (A) Superposition of the whole structures between G196S–TXA6101 (blue green), G196S (yellow), and WT T state (orange). (B) Close-up view of the inhibitor-binding site. The mF_o–DF_c omit map is contoured at 3.0 σ as a gray mesh. Anomalous difference map is contoured at 5.0 σ as a magenta mesh.

As observed in the TXA6101 and TXD1107 complexes with WT SaFtsZ, the bromo group on the oxazole ring of TXA6101 interacts with the hydrophobic pocket formed by Leu261, Asn263, Thr309, and Ile311 (Fig. 2-4B). This interaction strongly fixes the orientation of the oxazole ring and dominantly determines the position of the CF$_3$-phenyl ring. A rotatable single-bond between the phenyl and oxazole rings of TXD1107 enables the two rings to interact with the C$_\beta$ atom of the Ser196 side chain, which allows the compound to bind SaFtsZ G196S mutant without steric clash (Fig. 2-6A, B). Unlike the oxazole and phenyl rings of TXA6101, the corresponding thiazole and pyridyl rings of TXA707 are fused. Note that this thiazolopyridine ring of TXA707 is supported by tight Van der Waals interactions by the four hydrophobic residues (Fig. 2-4A). As a result, TXA707 cannot avoid a steric clash between the nitrogen atom on the thiazole ring of the compound and Ser196 (Fig. 2-6A, C). These results suggest that structural flexibility depending on the presence or absence of a single bond linking the five-membered and six-membered rings determines the ability of the inhibitor to target the G196S mutant protein.
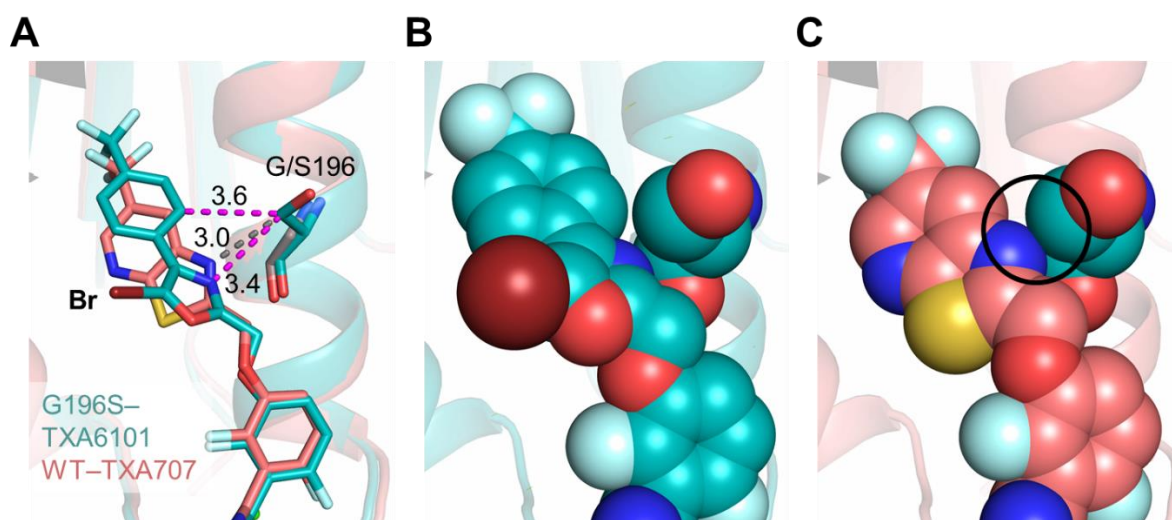
Figure 2-6. Interaction between the inhibitors and Ser196. (A) Superposition of G196S–TXA6101 (blue green) and WT–TXA707 (pink) complex structures. Van der Waals contacts and steric crash are shown by magenta and gray dotted lines, respectively. The distances are labeled in Å. (B, C) Sphere representation of the inhibitors and Ser196 in G196S–TXA6101 (B) and WT–TXA707 (C) complex. Steric crash is highlighted by black circle in (C).

2.4. Summary

In this chapter, the author determined the crystal structures of SaFtsZ–inhibitor complexes. All of the inhibitors used in this study adopt the novel bent conformation. Newly identified inner hydrophobic pocket was found to accommodate CF_3 group and to enable further structure optimization of the inhibitors. The author also determined the crystal structure of one of the most frequently observed drug resistant mutant G196S in complex with TXA6101, and revealed that the interactions including bromo group and the increased structural flexibility of the inhibitor are key factors for overcoming the drug resistance mutations in SaFtsZ. These findings offer a structural basis for the design of new FtsZ inhibitors with enhanced antibacterial potency and a reduced susceptibility to mutational resistance.

Chapter 3

Dynamic Behavior of FtsZ Filaments Visualized

by High-Speed AFM

3.1. Introduction

As mentioned throughout General Introduction, the imaging studies on visualizing FtsZ protofilaments and the Z-rings, mainly employing fluorescence, electron, and atomic force microscopy, have greatly contributed to identify the roles and features of dynamic FtsZ protein. Especially, AFM has been widely used to investigate the dynamic behavior of FtsZ, although a time scale is limited above a minute (79-82). From both scientific and medical points of view, the interest also goes to how the inhibitors affect FtsZ dynamic properties: polymerization, bending, forming bundles and rings, and dissociation. A previous electron microscopic study reported that PC190723 enhances the formation of polymers and further bundles, coils, and toroids in FtsZ from *B. subtilis* and SaFtsZ (50). High-speed AFM developed by Dr. Toshio Ando and co-workers at Kanazawa University (83, 84) has been expected to be a powerful tool for visualization of FtsZ polymer dynamics at much faster frame rate (~1 frame s^{-1}), and it succeeded in capture polymer dynamics of FtsZ from *E. coli* on a time scale of several seconds (85). However, this study mainly focuses on ClpX, an ATP-dependent chaperone and FtsZ modulator, and visualizes only after formation of high-density FtsZ filaments by pre-incubation on mica surface.

Here, the author visualized the formation and dissociation process of SaFtsZ filaments using high-speed AFM by adding FtsZ protein during the measurement. Straight and curved filaments were mainly formed in the absence and presence of the inhibitors, respectively. Lateral interaction between the filaments seems to be significant factor for the new filament growth in both cases. The difference of the filament shapes reflects that of the inhibitor activities.

3.2. Materials and Methods

3.2.1. Sample preparation

SaFtsZ$_{12-316}$ was cloned, expressed, and purified as described in section 1.2.1, except 5 ml HiTrapQ HP column (GE Healthcare) was used instead of Resource Q column. To decrease the effect of FtsZ-bound GDP, refolded SaFtsZ$_{12-316}$ was also tested. Consequently, no different feature was found between the no-refolded and refolded SaFtsZ. Refolded SaFtsZ was prepared as the non-refolded one, except the following additional denaturing and refolding steps were inserted after the anion exchange chromatography: the FtsZ fraction was dialyzed against denaturing buffer (50 mM Tris-HCl pH 7.5, 200 mM NaCl, 10% v/v glycerol, 6 M urea) for 2–3 h three times. The denatured sample was refolded by a dialysis against 50 mM Tris-HCl pH 7.5, 10 % v/v glycerol for 3 h. The refolded FtsZ was purified again using 5 ml HiTrapQ HP column, and the protein was eluted by a 30–750 mM NaCl gradient.

3.2.2. High-speed AFM measurement

All AFM images in this thesis were captured by a laboratory-built high-speed AFM apparatus in the tapping mode (83, 84). The cantilever (Olympus) shows a resonant frequency of ~1 MHz in water and a spring constant of ~0.16 N m^{-1}. The laser, whose output is ~0.8 mW and wavelength is 680 nm, was focused onto the back side of the cantilever, and the reflected laser deflection from the cantilever was detected with an optical beam deflection detector. To obtain higher resolution images, an amorphous carbon tip was constructed on the original AFM cantilever by electron beam deposition (83, 86). The observation was started on a freshly cleaved mica surface under a 70–80 μl of pool buffer (50 mM Tris-HCl pH 7.5, 5 mM MgCl$_2$, 100 mM KCl), and purified SaFtsZ, GTP, and GDP were added, if required, during the measurements. For observations of FtsZ–inhibitor complexes, FtsZ and the inhibitor dissolved in DMSO were mixed and pre-incubated on ice for 0.5–1 h. All measurements were performed at room temperature.

3.3. Results and Discussion

3.3.1. Formation and dissociation of the FtsZ filaments

In many previous AFM studies, high concentration of KCl (500 mM) has been included in the observation buffers (79-82). The author first tested various concentration of KCl, and found high KCl concentration promotes SaFtsZ adsorption to mica surface and rapid polymerization. To decrease the rate of polymerization and observe dissociation of FtsZ filaments, KCl concentration was reduced to 100 mM. All measurements below were performed under the pool buffer (50 mM Tris-HCl pH 7.5, 5 mM $MgCl_2$, 100 mM KCl), and GTP and GDP were added if required. Full-length SaFtsZ polymerizes at lower protein concentration and more rapidly than $SaFtsZ_{12–316}$, so the truncated construct were used below. Under this condition, many filaments were also observed in the presence of 600 μM GTP (Fig. 3-1A). Height profile along one filament (red line) obviously indicates the existence of periodic structure (Fig. 3-1B), and this period corresponds to the translation period (4.4 nm) of SaFtsZ filament in the crystal. Thus, the author confirmed that SaFtsZ also polymerizes and forms filaments in a similar manner to the crystal structure on bare mica.
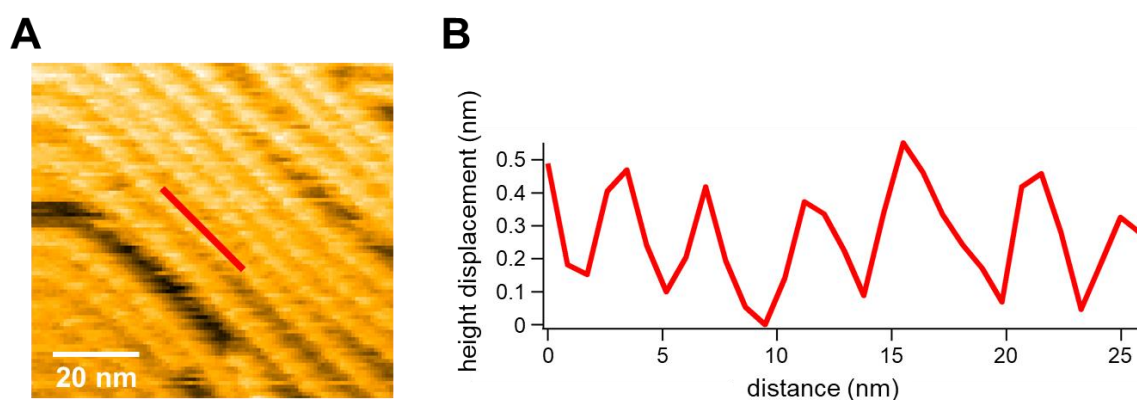
Figure 3-1. SaFtsZ filaments observed by high-speed AFM. (A) An image of SaFtsZ filaments in the presence of 600 μM GTP. (B) Profile of height displacement at the red-lined section in (A).

Next, FtsZ filaments formation process were investigated. AFM measurement was started under the pool buffer supplemented 600 μM GTP, and then 200 nM SaFtsZ was added after starting the

measurement. Initially, one filament grew straightforward, and then another filament extended along it (Fig. 3-2, 220–280 s). This result reflects the importance of lateral interaction between the FtsZ filaments for polymerization. Most of the FtsZ molecules form straight filaments. Some filaments grew in independent directions (300–400 s), but finally many filaments arranged in parallel (450 s). These rearrangements of FtsZ polymer orientation are also caused by the stable lateral interactions and can be observed because of the weakened interaction between FtsZ and mica surface by reducing KCl concentration in the pool buffer.
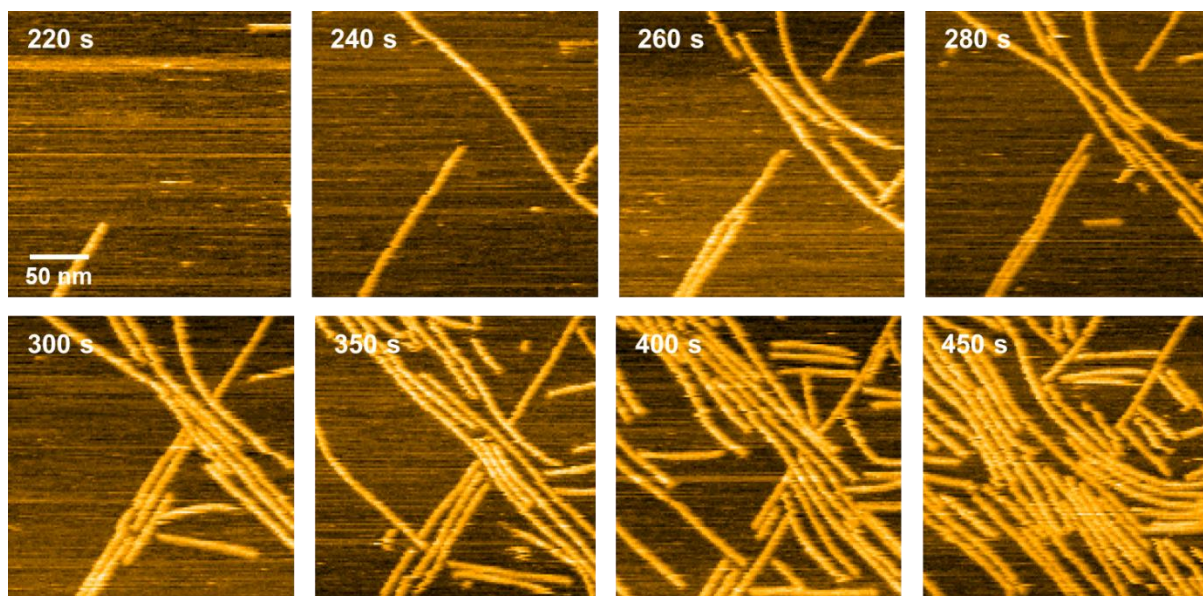
Figure 3-2. Growth of SaFtsZ straight filaments in the presence of 600 μM GTP.

Filament dissociation was also observed under the same buffer but supplemented an excess (6 mM) of GDP. In the beginning, high density filaments were formed in the presence of 600 μM GTP. Many gaps were found in the filaments in the presence of 3 mM GDP, but they were immediately repaired and filled in with free FtsZ monomers. This state is considered to be in equilibrium between dissociation and polymerization of the FtsZ filaments. In contrast, when the GDP concentration was increased to 6 mM (Fig. 3-3, 0 s), a number of gaps were observed in or between the filaments even after a time (100–200 s). Then the gaps expanded rapidly, leading to complete dissociation (300–580 s). This is probably

because FtsZ population in the R state was increased by GDP binding and the interaction between FtsZ monomers was weakened as described in section 1.3.1 (Fig. 1-4B, C); thereby the equilibrium was biased towards dissociation of the filaments. Note that filament bending was hardly observed even in the condition without the lateral interaction, which raises a question to the FtsZ filament bending model. *In vivo*, other requirements (e.g. flexible tethering by FtsA and support by other cell division proteins) may allow FtsZ filaments to bend by GDP binding. This result demonstrates how useful high-speed AFM is, because this is the first visualization of the dissociation process of high density FtsZ filaments in a second time scale, which has been considered difficult with AFM.
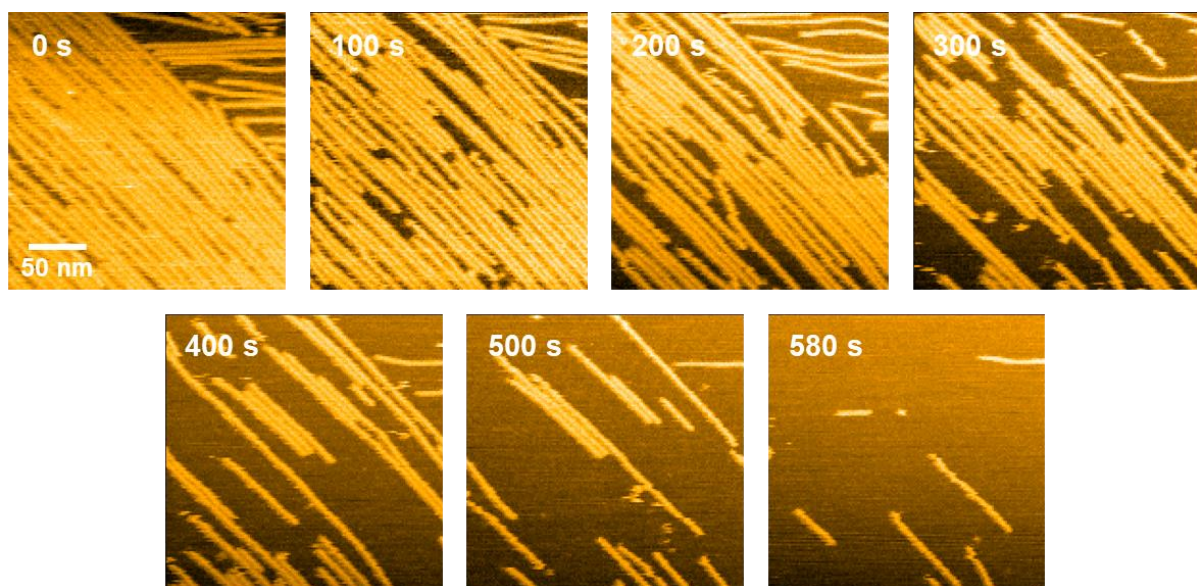
Figure 3-3. Dissociation of SaFtsZ filaments in the presence of 6 mM GDP.

3.3.2. Effects of inhibitors

Next the author investigated the effect of the inhibitors. 22.5 μM TXD1107, which shows the lowest MIC value (Table 2-1), was pre-incubated with SaFtsZ. Unlike the straight filaments in the absence of the inhibitors, a curved filament grew and then another filament was also curved along it (Fig. 3-4). Finally, many coils or toroids were generated. This result suggests that the inhibitor can also bind not only SaFtsZ filaments but also a monomer, because the filaments were generated in a curved form from the beginning, not bending after growing straightforward. Surprisingly, the curved filaments

can be formed without adding GTP, probably because the binding of the inhibitor fixes SaFtsZ conformation to the T state even in the GDP-bound form and promotes polymerization. Judging from the crystal structure, intermolecular interaction in the GDP-bound T state is enough strong to polymerize, but the curved filament found here is apparently different from the straight one observed in the crystal structure. As described in Chapter 2, the crystal structures in the T state of inhibitor-free and inhibitor-bound form are structurally identical, because the inhibitors were introduced by a soaking method. Otherwise, only straight filaments could be observed in SaFtsZ crystals due to the crystal packing, so the possibility cannot be excluded that the inhibitors bind and fix FtsZ to another T state-like conformation stabilizing the interaction in the curved filament, not to the T state conformation observed in the crystal.
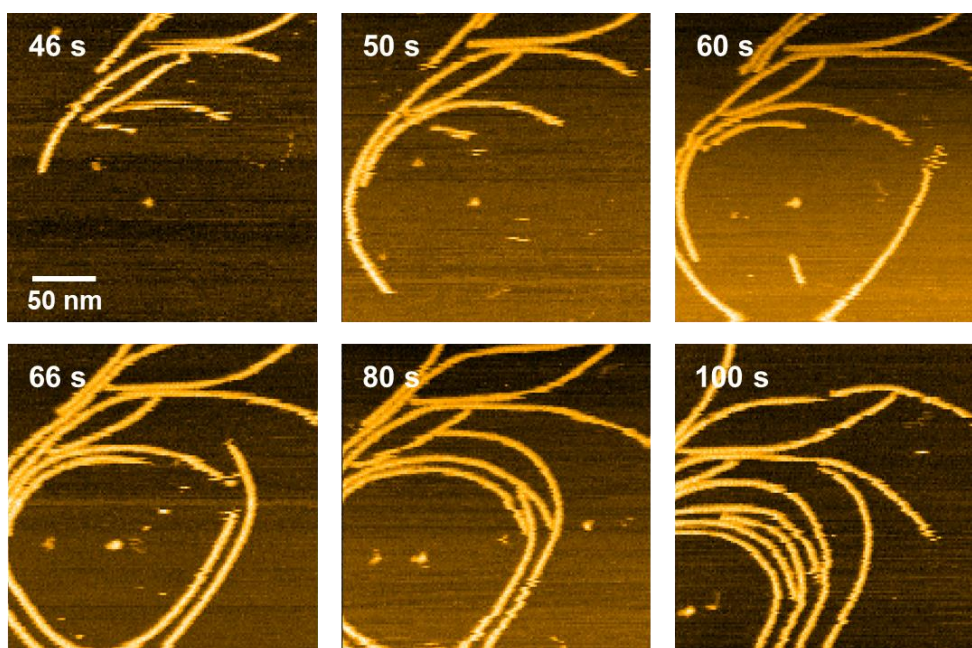
Figure 3-4. Growth of SaFtsZ curved filaments in the presence of 22.5 μM TXD1107 and in the absence of GTP.

Finally, the author also tested other inhibitors (PC190723 and TXA707) and G196S mutant. In WT SaFtsZ, all inhibitor-bound FtsZ shows many coiled structures, but in TXA707, FtsZ seems to assemble in a shorter filaments (Fig. 3-5B) than those in the other inhibitors (Fig. 3-5A, C). This tendency might reflect the slightly higher MIC value of TXA707 (1 μg ml^{-1}) (Table 2-1). However, in G196S mutant,

similar coiled structures were observed only in the presence of TXD1107 (Fig. 3-5F), and the others

show a number of straight filaments observed in the absence of the inhibitors (Fig. 3-5D, E). These

results obviously correlate with that of the MIC assay because TXA707 and PC190723 lack inhibitory

activity against SaFtsZ G196S (Table 2-1). In addition, filaments were hardly observed in the absence

of GTP in the mutant even in the presence of TXD1107. The MIC values partially explain this result:

TXD1107 shows much lower value against G196S mutant (1 μg ml^{-1}) than that against WT FtsZ (0.125

μg ml^{-1}), although still active against the mutant. One question still remains: why WT SaFtsZ with

TXA707 polymerizes even in the absence of GTP despite the same MIC value (1 μg ml^{-1})? It was

reported that FtsZ assembly cooperativity is affected by the addition of PC190723 (49), but this property

could not be investigated in AFM measurement or MIC assay. Further studies are needed to elucidate

the factors underlying these results, which is affected by the inhibitors and the mutation.
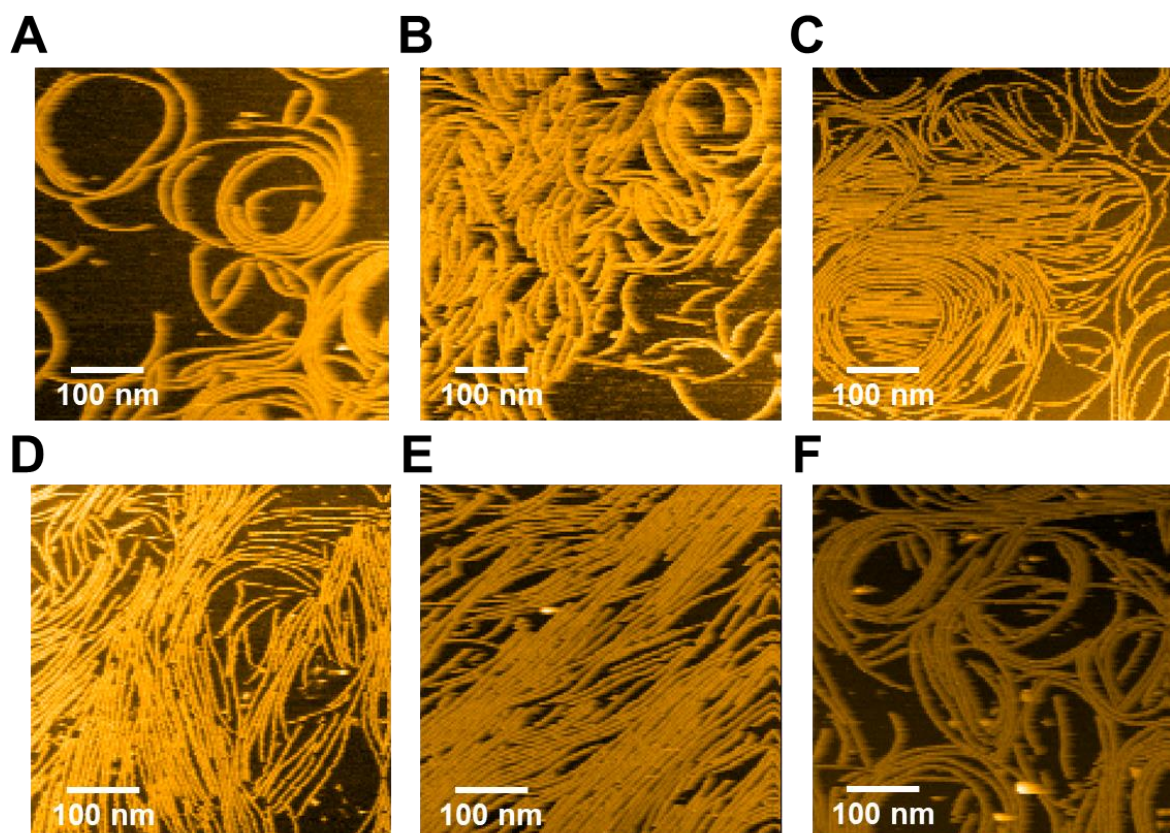
Figure 3-5. Effects of the inhibitors. Filament images of SaFtsZ WT in the absence of GTP (A, B, C) and G196S mutant in the presence of 1 mM GTP (D, E, F) are shown. 22.5 μM PC190723 (A, D) or TXA707 (B, E) or TXD1107 (C, F) were pre-incubated with SaFtsZ.

3.4. Summary

In this chapter, the author visualized the formation and dissociation process of SaFtsZ filaments using high-speed AFM. Straight and curved filaments were predominantly generated in the absence and presence of the inhibitors, respectively. Lateral interaction between the filaments triggers the formation of a new filament in both cases. The filament shapes strongly correlate with the results of MIC assay, but several disagreements between the filament structures observed in the crystals and by the AFM measurements remain to be elucidated.

Chapter 4

Crystallographic and Interaction Analysis of FtsA

4.1. Introduction

As described in section 0.2, understanding of the molecular function of FtsA during cell division has been hindered by limited structural information of FtsA. The only available crystal structure is TmFtsA from hyperthermophilic bacteria *Thermotoga maritima* (33, 42), so it is worth acquiring structural information of FtsA from other organism, especially mesophilic bacteria, for highlighting common and intrinsic features. However, previous studies suggest that FtsA from *E. coli* and *P. aeruginosa* need refolding in a purification step and seem to be difficult to prepare high-quality sample suitable for crystallization (37, 38). FtsA as well as FtsZ should be an attractive target for drug development due to its essentiality and wide conservation among bacterial species. Actually, in FtsA from *P. aeruginosa*, peptide screenings by phage display was performed, acquiring several peptide inhibitors (37). Structural information of FtsA from pathogenic bacteria should be useful in terms of the inhibitor design.

FtsA interacts with FtsZ C-terminus and the interaction is also essential for complete cell division, which may highlight the possibility of protein-protein interaction (PPI) inhibitor development. Previous mutational studies suggest Crystal structure of TmFtsA in complex with the C-terminus peptide of TmFtsZ offers the information about binding manner of FtsZ (33). The previous mutational study using FtsZ and FtsA from both *S. aureus* and *E. coli* represents the importance of a conserved residues in the C-terminus of FtsZ for FtsZ–FtsA interaction (29). Interestingly, the extreme C-terminus of SaFtsZ has an extra non-conserved Arg-rich sequence (RRSRRTRR), but it was not described in the previous study.

Here, the author discovered that SaFtsA is amenable to overexpression in *E. coli* and can be purified without refolding steps. SaFtsA also produce a diffraction-quality crystal with β-γ-imidoadenosine 5'-phosphate (AMPPNP: a non or slowly-hydrolyzable ATP analog) and allows the

structure determination at 2.2 Å resolution. In the crystal, the SaFtsA molecules stack head to tail forming continuous filaments, as does TmFtsA. However, SaFtsA filaments are twisted in two different torsion angles, and they align in antiparallel. A hairpin region of TmFtsA involved in intermolecular interactions is found to be more rigid than that of SaFtsA because of more hydrogen bonds existence. In addition, we demonstrated that SaFtsZ and SaFtsA form a stable complex *in vitro*, and confirmed the essentiality of the Arg-rich region for FtsZ–FtsA complex formation.

4.2. Materials and Methods

4.2.1. Cloning, expression, and purification of SaFtsA and SaFtsZ

SaFtsA (UniProt ID: Q6GHQ0) was cloned, expressed, and purified in the following method. The *ftsA* gene was amplified from the genomic DNA of *S. aureus* (ATCC accession No. 43300) using the following primers: forward, 5'-GCCATATGGAAGAACATTACTACGTAAG-3', reverse, 5'-GCGGATCCTCATTCAAATAGAGATTTCATTAG-3'), and was subcloned into the vector pCR4-TOPO (Invitrogen) with a TOPO TA cloning kit (Invitrogen). The sequence was verified by sequencing. Recloning into the vector pColdI (TaKaRa Bio) was performed via the restriction sites *NdeI* and *BamHI*, resulting in the addition of an N-terminal 6×His-tag and Factor Xa protease cleavage site with the sequence MNHKVHHHHHHIEGRH. The resulting plasmid was transformed into *E. coli* DH5α and successful plasmids were selected by colony PCR and extracted using a QIAprep Spin Miniprep Kit (QIAGEN). The plasmid was transformed into *E. coli* BL21(DE3) cells and the cells were cultured in LB medium supplemented with 100 μg ml^{-1} ampicillin at 37 °C. Expression was induced at an OD$_{600}$ of 0.5 with cooling to 15 °C and the addition of IPTG to a final concentration of 0.5 mM. Cells were harvested by centrifugation for 20 min at 12 000×g and 4 °C after 24 h of expression and were stored at −80 °C. FtsA cell pellets were resuspended in lysis buffer (50 mM Tris-HCl pH 7.5, 300 mM NaCl, 20 mM imidazole) with one tablet of protease-inhibitor cocktail (EDTA-free, Roche) per 50 ml of buffer, lysed using an EmulsiFlex-C3 homogenizer (Avestin) and centrifuged for 30 min at 100,000×g and 4 °C. The supernatant was filtered using a 0.45 μm syringe filter (Sartorius) and applied onto a 5 ml

HisTrap HP column (GE Healthcare). FtsA with an N-terminal 6×His-tag was eluted by a 45–310 mM imidazole gradient. Fractions containing FtsA were diluted ten times with a buffer consisting of 50 mM Tris-HCl pH 7.5 and loaded onto a 5 ml HiTrapQ HP column (GE Healthcare). FtsA was eluted with a 30–750 mM NaCl gradient. The FtsA fractions were further purified using a HiLoad 16/60 Superdex 200 prep-grade column (GE Healthcare) equilibrated with gel-filtration buffer (20 mM Tris-HCl pH 7.5, 150 mM NaCl). The 6×His-tag was not cleaved. The purity of the product was confirmed by SDS-PAGE and matrix-assisted laser desorption/ionization–time of flight mass spectrometry (MALDI-TOF MS, autoflex III, Bruker). The purified protein was concentrated to 10 mg ml^{-1}, flash-frozen in liquid nitrogen and immediately stored at −80 °C. SaFtsZ (UniProt ID: Q6GHP9) was cloned, expressed, and purified as reported for SaFtsA except that the cloning primers were: forward, 5'-GCCATATGTTAGAATTTGAACAAGGATTTAATC-3', reverse, 5'-GCGGATCCTTAACGTCTTGTTCTTCTTGAACG-3'. Selenomethionine-labeled SaFtsA (SeMet-SaFtsA) was expressed and purified with the same protocols as WT SaFtsA, except that the expression system was E. coli B834 (DE3) (Invitrogen) and that the cells were cultured in LeMaster medium, 50 mg l^{-1} SeMet, 100 μg ml^{-1} ampicillin, 5 ml l^{-1} vitamin solution as reported (87, 88). As assessed by MALDI-TOF MS, six of the possible seven methionines are present in SeMet-SaFtsA (SaFtsA: observed, 54,679 Da; calculated, 54,703 Da; SeMet-SaFtsA: observed, 54,962 Da; full substitution: calculated, 55,031 Da). Deletion mutagenesis of SaFtsZΔC (residues 1–382, eight amino acids from the C-terminus were truncated) was performed by inverse-PCR using KOD-plus (TOYOBO) and the following primers: forward, 5'-GGATCCGAATTCAAGCTTGTCGACC-3', reverse, 5'-TTATTCTTCTCTATTTCTAATGAAGCTAGGAATATC-3'. SaFtsZΔC was expressed and purified with the same protocols as WT SaFtsZ.

4.2.2. Crystallization, data collection and structure determination

Crystallization drops consisting of 0.5 μl 10 mg ml^{-1} SaFtsA solution and 0.5 μl reservoir solution were equilibrated against 60 μl reservoir solution. A needle-like crystal was obtained by mixing protein

solution consisting of 10 mg ml^{-1} SaFtsA, 1 mM AMPPNP (β-γ-imidoadenosine 5'-phosphate), 2 mM MgCl$_2$ with 0.2 M NaBr, 20% (w/v) polyethylene glycol 3350 (PEG3350). This condition was further optimized using the sitting-drop vapor-diffusion technique. A diffraction-quality SaFtsA crystal was obtained after two weeks by mixing 1 μl of the protein solution with 1 μl of a precipitant solution consisting of 0.15 M NaBr, 14.3% (w/v) PEG3350, 0.075 M Tris pH 7.8 and equilibrating against 1 ml of a reservoir solution consisting of 0.2 M NaBr, 19% (w/v) PEG3350, 0.1 M Tris pH 7.8. SaFtsA was also crystallized in the presence of ADP by mixing an equal volume (1 μl) of protein solution (10 mg ml^{-1}) containing 1 mM ADP and 2 mM MgCl$_2$ with 0.2 M lithium nitrate, 20% (w/v) PEG3350, 0.1 M sodium cacodylate, pH 7.0 (reservoir solution) and equilibrating against 1 ml of the reservoir solution. The crystallization conditions for SeMet-SaFtsA were the same as those for crystallization of SaFtsA in the presence of AMPPNP. The crystals were cryoprotected by changing PEG3350 concentration to 37% (w/v) and adding 15% (w/v) PEG8000, and individually mounted in a loop and then flash frozen in a stream of nitrogen at 100 K. Synchrotron-radiation diffraction data were collected at 100 K at the SPring-8 BL44XU (Hyogo, Japan) and Photon Factory BL-1A beamlines (Tsukuba, Ibaraki, Japan). The diffraction datasets were processed using HKL2000 (54). The structure of SaFtsA was determined by the single-wavelength anomalous diffraction method using SeMet-labeled-SaFtsA. Of the 24 possible selenium atoms in an asymmetric unit, 17 were found by SHELXD (89) using the anomalous signals in the SeMet-SaFtsA peak datasets. Initial phases were calculated and refined using SHELXE (89) and the graphical interface HKL2MAP (90). The model structures were refined with CNS (57, 58) and PHENIX (76), with manual inspection and modification in conjunction with the CCP4 program COOT (59). Data collection, phasing, and refinement statistics are summarized in Table 4-1. The refined structures were validated with PROCHECK (91). Chain interactions were assessed at the PISA server (61), and interface interactions were identified by LIGPLOT (62). The final atomic coordinates and structure factor amplitudes have been deposited in the RCSB Protein Data Bank (PDB entries: 3WQT and 3WQU). Figures were prepared using PyMOL (Schrödinger) and ESPript (65).

Table 4-1. Data collection and refinement statistics.

Data set	SaFtsA (AMPPNP)	SaFtsA (ATP)	SaFtsA (SeMet)
PDB entry	3WQT	3WQU	
Data collection			
X-ray Source	Photon factory BL1A	SPring-8 BL44XU	SPring-8 BL44XU
Wavelength (Å)	1.000	0.900	0.979
Space group	$P2_1$	$P2_1$	$P2_1$
Unit-cell parameters			
a, b, c (Å)	75.26, 102.74, 105.86	82.53, 122.02, 107.00	74.54, 101.87, 105.37
β (°)	96.54	95.66	96.23
Resolution (Å)	38.0–2.20 (2.24–2.20)[1]	39.7–2.80 (2.85–2.80)	50.0–2.70 (2.75–2.70)
Total reflections	234,088	196,794	334,143
Unique reflections	78,940	47,837	84,991
Completeness (%)	97.4 (97.4)	92.3 (86.5)	100.0 (100.0)
I/σ	18.6 (2.1)	18.7 (2.2)	14.7 (1.6)
R_{merge}[2] (%)	6.7 (39.6)	7.5 (59.3)	10.0 (58.5)
Phasing			
No. of sites			17
FOM[3]			0.32
Refinement			
Resolution (Å)	38.0–2.20	39.7–2.80	
$R_{\mathrm{work}}/R_{\mathrm{free}}$[4] (%)	23.4/28.9	20.7/25.4	
No. of molecules in the A.U.	4	4	
No. of atoms			
Protein	11,051	11,487	
Ligand	139	128	
Water	428	48	
Average B-factors (Å^2)			
Protein	49.0	60.4	
Ligand	40.7	46.5	
Water	44.5	47.2	
RMSD from ideal			
Bond length (Å)	0.007	0.009	
Bond angles (°)	1.2	1.3	

[1]Values in parentheses are for the highest resolution shells.

[2]$R_{\mathrm{merge}} = \Sigma_{hkl} \Sigma_i |I_i(hkl) - <I(hkl)>|/\Sigma_{hkl} \Sigma_i I_i(hkl)$, where $I_i(hkl)$ is the intensity of an individual reflection and $<I(hkl)>$ is the mean intensity of symmetry-equivalent reflections.

[3]Figure of merit $= |F(hkl)\mathrm{best}|/|F(hkl)|$; $F(hkl)\mathrm{best} = \Sigma_\alpha P(\alpha) F_{hkl}(\alpha)/\Sigma_\alpha P(\alpha)$.

[4]$R_{\mathrm{work}} = \Sigma_{hkl} ||F_{\mathrm{obs}}| - |F_{\mathrm{calc}}||/\Sigma_{hkl} |F_{\mathrm{obs}}|$, where F_{obs} and F_{calc} are observed and calculated structure-factor amplitudes, respectively. R_{free} was calculated as for R_{work} but using only 5% unrefined subset of reflection data.

4.2.3. Size-exclusion chromatography

Each sample was concentrated to 10 mg ml^{-1} and supplemented with 5 mM MgCl$_2$. For the complexes, SaFtsZ (or SaFtsZΔC) and SaFtsA were mixed and supplemented with MgCl$_2$, and then incubated at 20 ℃ for 20 min. A volume of 300 μl (600 μl for the complexes) was applied onto a HiLoad 16/60 Superdex 200 prep-grade column (GE Healthcare) and eluted with the gel-filtration buffer. Each peak was further analyzed by SDS-PAGE.

4.2.4. Native-PAGE

Each sample was diluted to 2 mg ml^{-1} and supplemented with 2 mM MgCl$_2$. For the complexes, SaFtsZ (or SaFtsZΔC) and SaFtsA were mixed and supplemented with MgCl$_2$. All samples were mixed with an equal volume of 2X sample buffer (10 mM Tris-HCl pH 7.5, 50% v/v glycerol, 1 mg ml^{-1} bromophenol blue) and incubated on ice for 20 min before loading onto 10% polyacrylamide gel. The electrophoresis was performed at 40 mA/gel and 4 ℃.

4.3. Results and Discussion

4.3.1. Crystal structure of SaFtsA

Crystal structures of SaFtsA complexed with AMPPNP and ATP were determined at 2.2 and 2.8 Å resolution, respectively. The structures are superposed well (RMSA = 0.32 Å for aligned 351 C$_\alpha$ atoms) and no significant structural change was observed, so only higher-resolution AMPPNP-complexed structure is described below. The overall structure of SaFtsA resembles that of TmFtsA (33, 42) and shares the canonical actin-like fold. The SaFtsA monomer consists of four domains, 1A, 1C, 2A, and 2B, and a difference Fourier omit map clearly shows that AMPPNP is bound in the pocket formed by domains 1A, 2A, and 2B (Fig. 4-1). The adenine ring of AMPPNP is stabilized by the side chain of His255 via a π-π stacking. The side chains of Glu251, Lys254, and His255 interacts with the ribose moiety. Two loops participate in the binding of the phosphates: S1–S2 loop (residues 13–17) and S9–S10 loop (residues 209–211). Mg^{2+} ion was observed to bridge between P$_\beta$ and P$_\gamma$ oxygens. In addition,

two water molecules (labeled W1 and W2) are located in 4.5 and 4.7 Å distance from the P_γ atom, and the β-γ-bridging oxygen-P_γ-water angles are 139° and 133°, respectively. In TmFtsA structures, the water molecule corresponding to W1 is located in 4.3–4.6 Å distance from the P_γ atom and the angle is 113–135°, and W2 is replaced by the side chain of Ser84. These distances and angles suggest that the positions of W1 and W2 are not suitable for ATP hydrolysis. Indeed, SaFtsA shows little ATPase activity (see below). However, some previous studies suggested that FtsA may exhibit actin-like ATPase activity (36, 37). One of the possibility is that FtsA-interacting proteins induce structural changes of FtsA to increase its ATPase activity during cell division.
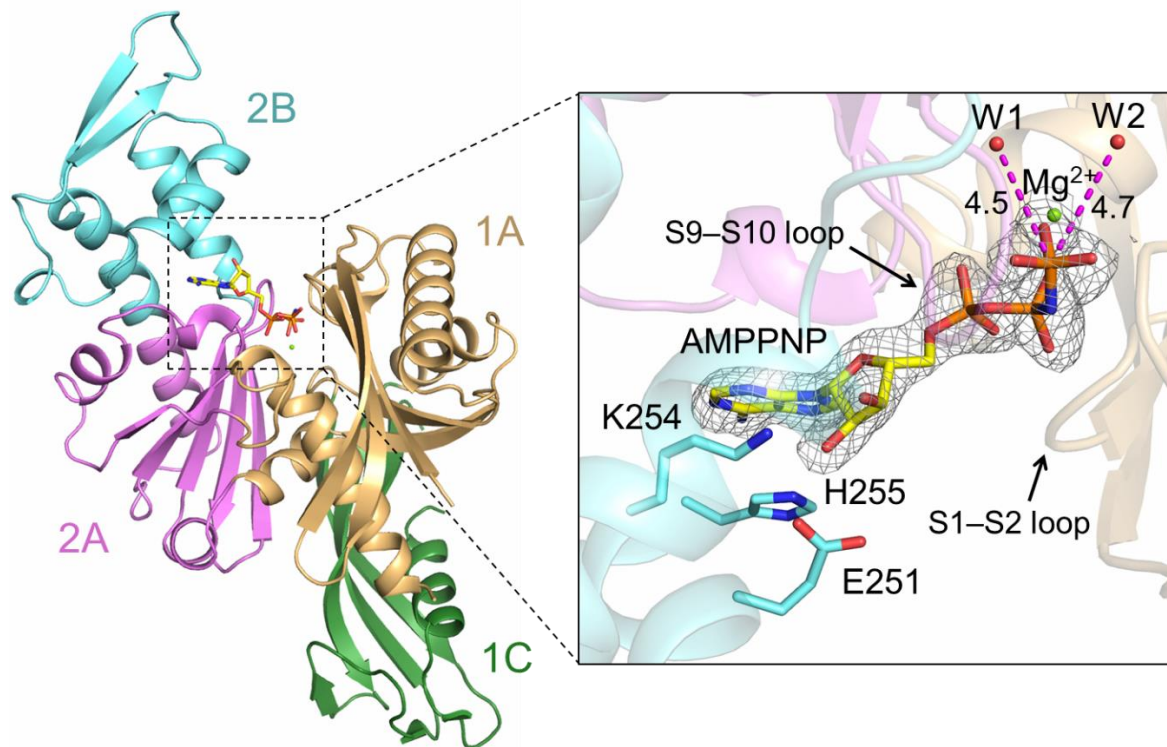
Figure 4-1. Overall structure of SaFtsA. Domains 1A, 1C, 2A, and 2B are colored in light orange, green, pink, and cyan, respectively. The mF_o–DF_c omit map is contoured at 3.0 σ as a gray mesh in the right panel. The distances are labeled in Å.

The crystallographic asymmetric unit contains four SaFtsA molecules (chains A, B, C, and D). The A, B and C, D molecules stack head to tail in the crystal to form two antiparallel filamentous structures (Fig. 4-2). One chain and the same chain in the neighboring asymmetric unit are related by a 106 Å translation. The two molecules in the head-to-tail dimer (A–B and C–D) are twisted 28° (A–B) and 17°

(C–D). These interaction is mainly mediated by two interfaces: 1A–1C and 2B–2A interfaces (Fig. 2, red and blue circles, respectively). The 1A–1C interface has a relatively large area (564 Å^2) compared with the 2B–2A interface (174 Å^2). The 1A–1C interactions are essentially conserved in the A, B and C, D interfaces. This interface includes Leu145, corresponding to Met147 in *B. subtilis* FtsA, whose importance for polymerization is confirmed by mutational study (33). The 2B–2A interactions are mediated by a few residues in the S12–S13 hairpin loop, H8–S14 loop, and H10–S15 loop, and the interactions are not conserved well in the A, B and C, D interfaces. Although helical filament can be generated by superposing A–B or C–D SaFtsA dimers one by one, in contrast to straight TmFtsA filament in the crystals, whether this twist is required for functions of FtsA remains to be elucidated.
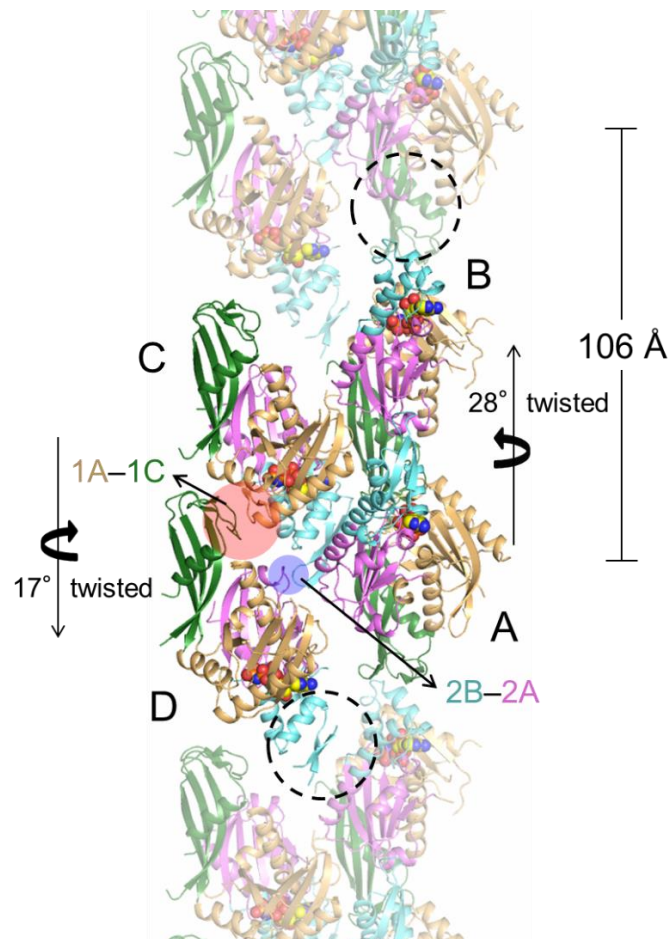
Figure 4-2. Crystal packing of SaFtsA. Domains are colored as Fig. 4-1. The molecules in neighboring asymmetric units are shown in semi-transparent. AMPPNP molecules are represented by spheres. A period of the dimer units (A–B or C–D) and the twist angles are represented. 1A–1C and 2B–2A interfaces are shown in red and blue circles, respectively. Structural disorders of the S12–S13 hairpin in B and D chains are highlighted by dashed circles.

The S12–S13 hairpin is structurally ordered in A and C molecules, whereas it is disordered in B and D molecules, which reflects the increased flexibility of this region compared to the corresponding region of TmFtsA (Fig. 4-2). This hairpin seems to be important for the interactions with other molecules, because the mutation point of FtsA[*] (R286W, a gain-of-function mutant of EcFtsA (39)) is located in the S12–S13 hairpin. Additionally, the S13–H8 region of SaFtsA is considered to be binding site of the C-terminus of SaFtsZ, based on the structure of the TmFtsA–FtsZ C-terminal peptide complex (PDB entry: 4A2A, Fig. 4-3A) (33). Therefore, the S12–S13 hairpin should be important for FtsA function and partner proteins binding. The position of S12–S13 hairpin of SaFtsA is clearly different from that of TmFtsA, probably because the TmFtsA S12–S13 hairpin is stabilized by more hydrogen bonds than SaFtsA (Fig. 4-3B, C).
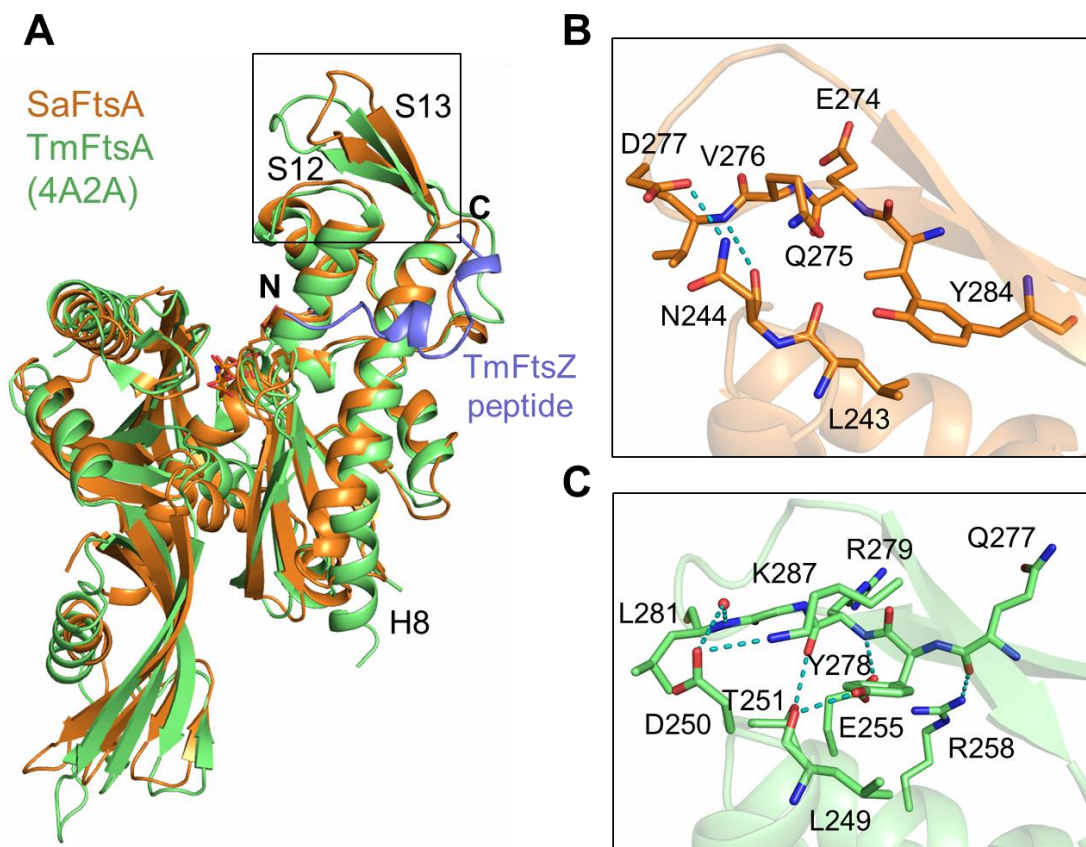
Figure 4-3. Structure comparison of S12–S13 hairpin. (A) Superposition of SaFtsA (orange) and TmFtsA–FtsZ complex (PDB entry: 4A2A, green) structures. The C-terminal peptide of SaFtsZ is shown in blue. (B, C) Close-up views of the S12–S13 hairpin of SaFtsA (B) and TmFtsA (C). Water molecules are shown by red spheres. Hydrogen bonds are shown by cyan dotted lines.

4.3.2. SaFtsZ–FtsA interaction assays

FtsZ is known to bind FtsA through its C-terminal region (30, 92). SaFtsZ has an extra unique Arg-rich sequences in its extreme C-terminus (Fig. 4-4A, red box). This region did not be focused well in the previous SaFtsZ–FtsA interaction assay (29). Judging from the TmFtsA–FtsZ peptide structure, this region will be extended to near the S13–H8 region. SaFtsA has many acidic residues in S12–S13 hairpin (Glu274, Asp277, Asp279, and Glu280) and in the following H8 helix (Asp288, Asp291, Glu294, Glu298, and Glu299). Thus, it is suggested that electrostatic interactions among these residues promote the formation of SaFtsZ–FtsA complex. To confirm the importance of this Arg-rich region of SaFtsZ, SaFtsZ–FtsA complex formation were examined using full-length SaFtsZ and SaFtsZΔC, whose C-terminal eight residues (RRSRRTRR) were truncated, by the two methods: size-exclusion chromatography and Native-PAGE. SaFtsZ–FtsA complex is enough stable to be detected by size-exclusion chromatography (Fig. 4-4B, red line), but the peak corresponding to the complex was not observed in the case of SaFtsZΔC (Fig. 4-4B, green line). The Native-PAGE analysis showed the similar result that the band of the complex was disappeared when SaFtsZΔC and SaFtsA was loaded onto gel (Fig. 4-4C). These facts suggest that the extreme C-terminal Arg-rich region of SaFtsZ is quite important for binding SaFtsA. This extended interaction might be one of the reason why SaFtsZ–FtsA complex can be easily prepared by size-exclusion chromatography.
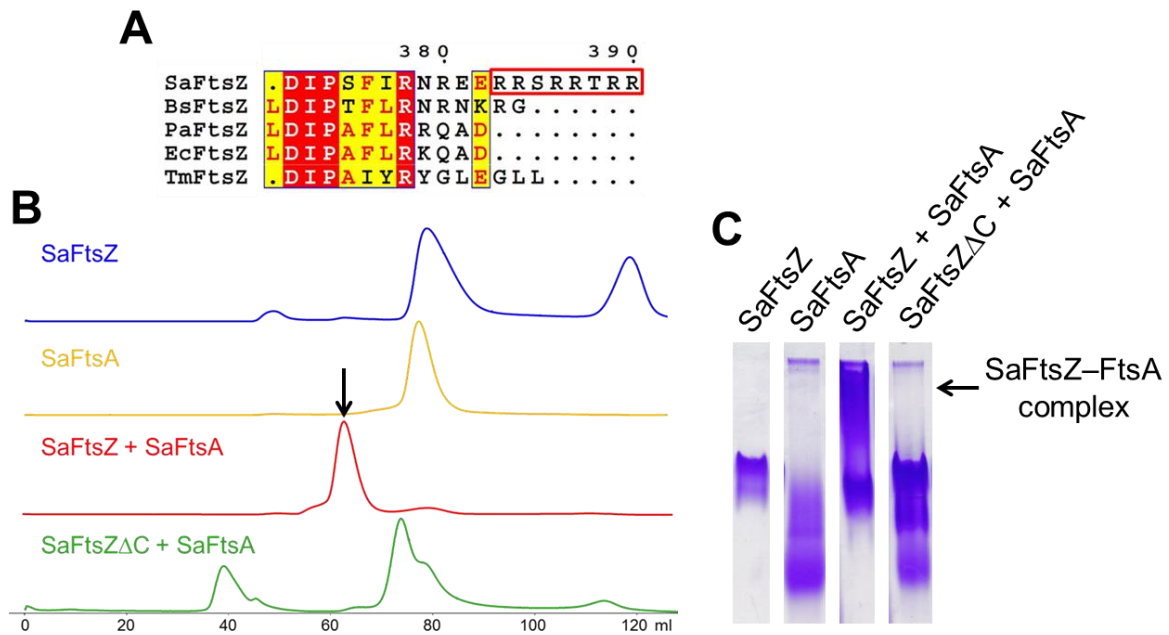
Figure 4-4. SaFtsZ–FtsA interaction assays. (A) Sequence alignment of FtsZ C-terminus. Arg-rich region is highlighted by a red box. (B) Elution profiles of size-exclusion chromatography on HiLoad 16/600 Superdex 200 prep grade. The peak corresponding to SaFtsZ–FtsA complex is indicated by a black arrow. (C) Complex formation analysis by Native-PAGE.

4.4. Summary

In this chapter, the author performed crystallographic analysis of SaFtsA. The SaFtsA molecules are aligned as twisted filaments in the crystal in contrast to the straight filaments of TmFtsA. The S12–S13 hairpin region, located near the FtsZ-binding region, shows different orientation compared to that of TmFtsA due to the less hydrogen bonds interactions. Moreover, SaFtsZ–FtsA interaction assays reveal that the C-terminal Arg-rich region of SaFtsZ is essential for SaFtsA binding. This unique interaction is probably responsible for the formation of the stable SaFtsZ–FtsA complex *in vitro*. This knowledge might be useful for inhibitor development which disrupts the SaFtsZ–FtsA interaction.

Conclusion

In Chapter 1, the author determined the crystal structures of non-mutated SaFtsZ in both the T and R state conformations in the same crystal for the first time, and proposed the mechanism of the T–R structural change. The transient structure and the significant interactions during the T–R conformational change were predicted by PaCS-MD simulation performed by the collaborators. Crystallographic analysis and conventional MD simulations using the key-interaction-disrupted mutant also supports these results. Intramolecular interaction was mainly focused in this study, and it would cooperate with the previously suggested intermolecular mechanism, which offers structural insights into the mechanism of T–R conformational change leading to the assembly/disassembly and the treadmilling of FtsZ molecules.

Disturbing the T–R conformational change is the effective strategy for drug development. In Chapter 2, the author determined the crystal structures of SaFtsZ in complex with the three inhibitors, TXA707, TXA6101, and TXD1107, developed based on this strategy. All of the inhibitors used in this study adopt the novel bent conformation, and newly identified inner hydrophobic pocket was found to allow further structure optimization of the inhibitors. The author also reported the crystal structure of the most frequently observed drug resistant mutant G196S in complex with TXA6101, and revealed that the existence of the bromo group and the enhanced structural flexibility of the inhibitor are key factors for overcoming the steric hindrance introduced by the drug resistance mutation in SaFtsZ. These results offer a structural basis for the design of new FtsZ inhibitors with increased antibacterial potency.

To investigate the effects of the novel inhibitors on FtsZ dynamics, high-speed AFM measurement was performed in Chapter 3. The author visualized the formation and dissociation process of SaFtsZ filaments by adding the protein during the measurement. Straight and curved filaments were predominantly generated in the absence and presence of the inhibitors, respectively, in accordance with the previous study. Lateral interaction between the filaments seem to promote the recruitment of FtsZ

monomer and the new filament formation in both cases. An extent of filament curvature strongly correlates with the inhibitory activity of the supplemented inhibitor, but several disagreements between the crystal structure and the AFM observation remain to be elucidated. Another factor, probably a kind of cooperativity, seem to underlie the dynamic FtsZ events.

FtsA is also essential player in bacterial cell division and attractive drug target, but its structural information has been significantly limited compared to FtsZ. Therefore, in Chapter 4, the author performed crystallographic analysis of SaFtsA. The molecules are aligned as two kinds of twisted antiparallel filaments in the crystal in contrast to the straight filaments observed in TmFtsA. The S12–S13 hairpin region, located near the FtsZ-binding region, shows different orientation and more flexibility compared to that of TmFtsA because of the less hydrogen bond interactions. Moreover, SaFtsZ–FtsA interaction assays indicate that the non-conserved C-terminal Arg-rich region of SaFtsZ is essential for SaFtsA binding. This unique interaction seems to assure the stable SaFtsZ–FtsA complex formation *in vitro*. This information might be a clue to the development of the SaFtsZ–FtsA interaction inhibitors.

Here, the author combines X-ray crystallographic analysis with several related methods to elucidate the molecular mechanism underlying bacterial cell division and establish structural basis for the development of antibacterial agent. For future perspective, MD simulations of the filamentous structures consisting of the T and R state molecules will be a powerful tool to further investigate the disparity between the crystallographic and microscopic result. Moreover, recent improvement of a resolution in cryo-electron microscopy may allow futuristic structure determination of FtsZ filament in biological condition and clear distinction between the T and R state in the filament. This research focused on SaFtsZ and SaFtsA in terms of drug development against MRSA, but the structural and other knowledge obtained in this study is a quite useful basis for discussing the similar and different features compared to the cell division proteins from other species, and a definite step for understanding the vast divisome machinery world.

References

(1) Antimicrobial Resistance: Global Report on Surveillance. (2014) World Health Organization, Geneva, Switzerland.

(2) Antibiotic Resistance Threats in the United States 2013. (2013) Centers for Disease Control and Prevention, Atlanta, GA.

(3) Sass, P. & Brötz-Oesterhelt, H. (2013) Bacterial Cell Division as a Target for New Antibiotics. *Curr. Opin. Microbiol.* **16**, 522–530.

(4) Haeusser, D. P. & Margolin, W. (2016) Splitsville: structural and functional insights into the dynamic bacterial Z ring. *Nature Reviews Microbiology* **14**, 305–319.

(5) Bramhill, D. & Thompson, C. M. (1994) GTP-dependent polymerization of *Escherichia coli* FtsZ protein to form tubules. *Proc. Natl. Acad. Sci. U. S. A.* **91**, 5813–5817.

(6) Mukherjee, A., Dai, K. & Lutkenhaus, J. (1993) *Escherichia coli* cell division protein FtsZ is a guanine nucleotide binding protein. *Proc. Natl. Acad. Sci. U. S. A.* **90**, 1053–1057.

(7) Bi, E. F. & Lutkenhaus, J. (1991) FtsZ ring structure associated with division in *Escherichia coli*. *Nature* **354**, 161–164.

(8) Scheffers, D. J., de Wit, J. G., den Blaauwen, T. & Driessen, A. J. M. (2002) GTP hydrolysis of cell division protein FtsZ: Evidence that the active site is formed by the association of monomers. *Biochemistry* **41**, 521–529.

(9) Lu, C., Stricker, J. & Erickson, H. P. (2001) Site-specific mutations of FtsZ--effects on GTPase and in vitro assembly. *BMC Microbiol.* **1**, 7.

(10) Löwe, J. & Amos, L. A. (1998) Crystal structure of the bacterial cell-division protein FtsZ. *Nature* **391**, 203–206.

(11) Wang, X. D., Huang, J. A., Mukherjee, A., Cao, C. & Lutkenhaus, J. (1997) Analysis of the interaction of FtsZ with itself, GTP, and FtsA. *J. Bacteriol.* **179**, 5551–5559.

(12) Sun, Q. & Margolin, W. (1998) FtsZ dynamics during the division cycle of live Escherichia coli cells. *J. Bacteriol.* **180**, 2050–2056.

(13) Lu, C., Reedy, M. & Erickson, H. P. (2000) Straight and curved conformations of FtsZ are regulated by GTP hydrolysis. *J. Bacteriol.* **182**, 164–170.

(14) Hsin, J., Gopinathan, A. & Huang, K. C. (2012) Nucleotide-dependent conformations of FtsZ dimers and force generation observed through molecular dynamics simulations. *Proc. Natl. Acad. Sci. U. S. A.* **109**, 9432–9437.

(15) Osawa, M., Anderson, D. E. & Erickson, H. P. (2009) Curved FtsZ protofilaments generate bending forces on liposome membranes. *EMBO J.* **28**, 3476–3484.

(16) Osawa, M., Anderson, D. E. & Erickson, H. P. (2008) Reconstitution of contractile FtsZ rings in liposomes. *Science* **320**, 792–794.

(17) Xiao, J. & Goley, E. D. (2016) Redefining the roles of the FtsZ-ring in bacterial cytokinesis. *Curr.*

Opin. Microbiol. **34**, 90–96.

(18) Yang, X., Lyu, Z., Miguel, A., McQuillen, R., Huang, K. C. & Xiao, J. (2017) GTPase activity-coupled treadmilling of the bacterial tubulin FtsZ organizes septal cell wall synthesis. *Science* **355**, 744–747.

(19) Bisson-Filho, A. W., Hsu, Y. P., Squyres, G. R., Kuru, E., Wu, F., Jukes, C., Sun, Y., Dekker, C., Holden, S., VanNieuwenhze, M. S., Brun, Y. V. & Garner, E. C. (2017) Treadmilling by FtsZ filaments drives peptidoglycan synthesis and bacterial cell division. *Science* **355**, 739–743.

(20) Oliva, M. A., Trambaiolo, D. & Löwe, J. (2007) Structural insights into the conformational variability of FtsZ. *J. Mol. Biol.* **373**, 1229–1242.

(21) Oliva, M. A., Cordell, S. C. & Löwe, J. (2004) Structural insights into FtsZ protofilament formation. *Nat. Struct. Mol. Biol.* **11**, 1243–1250.

(22) Leung, A. K., Lucile White, E., Ross, L. J., Reynolds, R. C., DeVito, J. A. & Borhani, D. W. (2004) Structure of *Mycobacterium tuberculosis* FtsZ reveals unexpected, G protein-like conformational switches. *J. Mol. Biol.* **342**, 953–970.

(23) Matsui, T., Yamane, J., Mogi, N., Yamaguchi, H., Takemoto, H., Yao, M. & Tanaka, I. (2012) Structural reorganization of the bacterial cell-division protein FtsZ from *Staphylococcus aureus*. *Acta Crystallogr. D Biol. Crystallogr.* **68**, 1175–1188.

(24) Matsui, T., Han, X., Yu, J., Yao, M. & Tanaka, I. (2014) Structural change in FtsZ Induced by intermolecular interactions between bound GTP and the T7 loop. *J. Biol. Chem.* **289**, 3501–3509.

(25) Li, Y., Hsin, J., Zhao, L., Cheng, Y., Shang, W., Huang, K. C., Wang, H. W. & Ye, S. (2013) FtsZ protofilaments use a hinge-opening mechanism for constrictive force generation. *Science* **341**, 392–395.

(26) Natarajan, K. & Senapati, S. (2013) Probing the conformational flexibility of monomeric FtsZ in GTP-bound, GDP-bound, and nucleotide-free states. *Biochemistry* **52**, 3543–3551.

(27) Martin-Garcia, F., Salvarelli, E., Mendieta-Moreno, J. I., Vicente, M., Mingorance, J., Mendieta, J. & Gomez-Puertas, P. (2012) Molecular dynamics simulation of GTPase activity in polymers of the cell division protein FtsZ. *FEBS Lett.* **586**, 1236–1239.

(28) Ramirez-Aportela, E., Lopez-Blanco, J. R., Andreu, J. M. & Chacon, P. (2014) Understanding nucleotide-regulated FtsZ filament dynamics and the monomer assembly switch with large-scale atomistic simulations. *Biophys. J.* **107**, 2164–2176.

(29) Yan, K., Pearce, K. H. & Payne, D. J. (2000) A conserved residue at the extreme C-terminus of FtsZ is critical for the FtsA-FtsZ interaction in Staphylococcus aureus. *Biochem. Biophys. Res. Commun.* **270**, 387–392.

(30) Ma, X. L. & Margolin, W. (1999) Genetic and functional analyses of the conserved C-terminal core domain of *Escherichia coli* FtsZ. *J. Bacteriol.* **181**, 7531–7544.

(31) Pichoff, S. & Lutkenhaus, J. (2005) Tethering the Z ring to the membrane through a conserved membrane targeting sequence in FtsA. *Mol. Microbiol.* **55**, 1722–1734.

(32) Bork, P., Sander, C. & Valencia, A. (1992) An ATPase domain common to prokaryotic cell cycle

proteins, sugar kinases, actin, and hsp70 heat shock proteins. *Proc. Natl. Acad. Sci. U. S. A.* **89**, 7290–7294.

(33) Szwedziak, P., Wang, Q., Freund, S. M. & Lowe, J. (2012) FtsA forms actin-like protofilaments. *EMBO J.* **31**, 2249–2260.

(34) Lara, B., Rico, A. I., Petruzzelli, S., Santona, A., Dumas, J., Biton, J., Vicente, M., Mingorance, J. & Massidda, O. (2005) Cell division in cocci: localization and properties of the Streptococcus pneumoniae FtsA protein. *Mol. Microbiol.* **55**, 699–711.

(35) Szwedziak, P., Wang, Q., Bharat, T. A., Tsim, M. & Löwe, J. (2014) Architecture of the ring formed by the tubulin homologue FtsZ in bacterial cell division. *Elife* **3**, e04601.

(36) Feucht, A., Lucet, I., Yudkin, M. D. & Errington, J. (2001) Cytological and biochemical characterization of the FtsA cell division protein of Bacillus subtilis. *Mol. Microbiol.* **40**, 115–125.

(37) Paradis-Bleau, C., Sanschagrin, F. & Levesque, R. C. (2005) Peptide inhibitors of the essential cell division protein FtsA. *Protein Eng. Des. Sel.* **18**, 85–91.

(38) Martos, A., Monterroso, B., Zorrilla, S., Reija, B., Alfonso, C., Mingorance, J., Rivas, G. & Jimenez, M. (2012) Isolation, characterization and lipid-binding properties of the recalcitrant FtsA division protein from Escherichia coli. *PLoS One* **7**, e39829.

(39) Geissler, B., Elraheb, D. & Margolin, W. (2003) A gain-of-function mutation in ftsA bypasses the requirement for the essential cell division gene zipA in Escherichia coli. *Proc. Natl. Acad. Sci. U. S. A.* **100**, 4197–4202.

(40) Osawa, M. & Erickson, H. P. (2013) Liposome division by a simple bacterial division machinery. *Proc. Natl. Acad. Sci. U. S. A.* **110**, 11000–11004.

(41) Loose, M. & Mitchison, T. J. (2014) The bacterial cell division proteins FtsA and FtsZ self-organize into dynamic cytoskeletal patterns. *Nat. Cell Biol.* **16**, 38–46.

(42) van den Ent, F. & Lowe, J. (2000) Crystal structure of the cell division protein FtsA from Thermotoga maritima. *EMBO J.* **19**, 5300–5307.

(43) Pichoff, S. & Lutkenhaus, J. (2007) Identification of a region of FtsA required for interaction with FtsZ. *Mol. Microbiol.* **64**, 1129–1138.

(44) Hurley, K. A., Santos, T. M., Nepomuceno, G. M., Huynh, V., Shaw, J. T. & Weibel, D. B. (2016) Targeting the Bacterial Division Protein FtsZ. *J. Med. Chem.* **59**, 6975–6998.

(45) Lappchen, T., Pinas, V. A., Hartog, A. F., Koomen, G. J., Schaffner-Barbero, C., Andreu, J. M., Trambaiolo, D., Lowe, J., Juhem, A., Popov, A. V. & den Blaauwen, T. (2008) Probing FtsZ and tubulin with C8-substituted GTP analogs reveals differences in their nucleotide binding sites. *Chem. Biol.* **15**, 189–199.

(46) Tan, C. M., Therien, A. G., Lu, J., Lee, S. H., Caron, A., Gill, C. J., Lebeau-Jacob, C., Benton-Perdomo, L., Monteiro, J. M., Pereira, P. M., Elsen, N. L., Wu, J., Deschamps, K., Petcu, M., Wong, S., Daigneault, E., Kramer, S., Liang, L., Maxwell, E., Claveau, D., Vaillancourt, J., Skorey, K., Tam, J., Wang, H., Meredith, T. C., Sillaots, S., Wang-Jarantow, L., Ramtohul, Y.,

Langlois, E., Landry, F., Reid, J. C., Parthasarathy, G., Sharma, S., Baryshnikova, A., Lumb, K. J., Pinho, M. G., Soisson, S. M. & Roemer, T. (2012) Restoring methicillin-resistant Staphylococcus aureus susceptibility to beta-lactam antibiotics. *Sci. Transl. Med.* **4**, 126ra135.

(47) Ohashi, Y., Chijiiwa, Y., Suzuki, K., Takahashi, K., Nanamiya, H., Sato, T., Hosoya, Y., Ochi, K. & Kawamura, F. (1999) The lethal effect of a benzamide derivative, 3-methoxybenzamide, can be suppressed by mutations within a cell division gene, ftsZ, in Bacillus subtilis. *J. Bacteriol.* **181**, 1348–1351.

(48) Haydon, D. J., Stokes, N. R., Ure, R., Galbraith, G., Bennett, J. M., Brown, D. R., Baker, P. J., Barynin, V. V., Rice, D. W., Sedelnikova, S. E., Heal, J. R., Sheridan, J. M., Aiwale, S. T., Chauhan, P. K., Srivastava, A., Taneja, A., Collins, I., Errington, J. & Czaplewski, L. G. (2008) An inhibitor of FtsZ with potent and selective anti-staphylococcal activity. *Science* **321**, 1673–1675.

(49) Elsen, N. L., Lu, J., Parthasarathy, G., Reid, J. C., Sharma, S., Soisson, S. M. & Lumb, K. J. (2012) Mechanism of action of the cell-division inhibitor PC190723: modulation of FtsZ assembly cooperativity. *J. Am. Chem. Soc.* **134**, 12342–12345.

(50) Andreu, J. M., Schaffner-Barbero, C., Huecas, S., Alonso, D., Lopez-Rodriguez, M. L., Ruiz-Avila, L. B., Nunez-Ramirez, R., Llorca, O. & Martin-Galiano, A. J. (2010) The antibacterial cell division inhibitor PC190723 is an FtsZ polymer-stabilizing agent that induces filament assembly and condensation. *J. Biol. Chem.* **285**, 14239–14246.

(51) Adams, D. W., Wu, L. J. & Errington, J. (2016) A benzamide-dependent ftsZ mutant reveals residues crucial for Z-ring assembly. *Mol. Microbiol.* **99**, 1028–1042.

(52) Harada, R. & Kitao, A. (2013) Parallel Cascade Selection Molecular Dynamics (PaCS-MD) to generate conformational transition pathway. *J. Chem. Phys.* **139**, 035103.

(53) Harada, R., Takano, Y., Baba, T. & Shigeta, Y. (2015) Simple, yet powerful methodologies for conformational sampling of proteins. *Phys. Chem. Chem. Phys.* **17**, 6155–6173.

(54) Otwinowski, Z. & Minor, W. (1997) Processing of X-ray diffraction data collected in oscillation mode. *Macromolecular Crystallography, Pt A* **276**, 307–326.

(55) McCoy, A. J., Grosse-Kunstleve, R. W., Adams, P. D., Winn, M. D., Storoni, L. C. & Read, R. J. (2007) Phaser crystallographic software. *J. Appl. Crystallogr.* **40**, 658–674.

(56) Murshudov, G. N., Skubak, P., Lebedev, A. A., Pannu, N. S., Steiner, R. A., Nicholls, R. A., Winn, M. D., Long, F. & Vagin, A. A. (2011) REFMAC5 for the refinement of macromolecular crystal structures. *Acta Crystallogr. D Biol. Crystallogr.* **67**, 355–367.

(57) Brunger, A. T. (2007) Version 1.2 of the Crystallography and NMR system. *Nat. Protoc.* **2**, 2728–2733.

(58) Brunger, A. T., Adams, P. D., Clore, G. M., DeLano, W. L., Gros, P., Grosse-Kunstleve, R. W., Jiang, J. S., Kuszewski, J., Nilges, M., Pannu, N. S., Read, R. J., Rice, L. M., Simonson, T. & Warren, G. L. (1998) Crystallography & NMR system: A new software suite for macromolecular structure determination. *Acta Crystallogr. D Biol. Crystallogr.* **54**, 905–921.

(59) Emsley, P. & Cowtan, K. (2004) Coot: model-building tools for molecular graphics. *Acta Crystallogr. D Biol. Crystallogr.* **60**, 2126–2132.

(60) Chen, V. B., Arendall, W. B., 3rd, Headd, J. J., Keedy, D. A., Immormino, R. M., Kapral, G. J., Murray, L. W., Richardson, J. S. & Richardson, D. C. (2010) MolProbity: all-atom structure validation for macromolecular crystallography. *Acta Crystallogr. D Biol. Crystallogr.* **66**, 12–21.

(61) Krissinel, E. & Henrick, K. (2007) Inference of macromolecular assemblies from crystalline state. *J. Mol. Biol.* **372**, 774–797.

(62) Wallace, A. C., Laskowski, R. A. & Thornton, J. M. (1995) LIGPLOT: a program to generate schematic diagrams of protein-ligand interactions. *Protein Eng.* **8**, 127–134.

(63) Hayward, S. & Berendsen, H. J. (1998) Systematic analysis of domain motions in proteins from conformational change: new results on citrate synthase and T4 lysozyme. *Proteins* **30**, 144–154.

(64) Thompson, J. D., Higgins, D. G. & Gibson, T. J. (1994) CLUSTAL W: improving the sensitivity of progressive multiple sequence alignment through sequence weighting, position-specific gap penalties and weight matrix choice. *Nucleic Acids Res.* **22**, 4673–4680.

(65) Robert, X. & Gouet, P. (2014) Deciphering key features in protein structures with the new ENDscript server. *Nucleic Acids Res.* **42**, W320–324.

(66) Ingerman, E. & Nunnari, J. (2005) A continuous, regenerative coupled GTPase assay for dynamin-related proteins. *Methods Enzymol.* **404**, 611–619.

(67) Fujita, J., Harada, R., Maeda, Y., Saito, Y., Mizohata, E., Inoue, T., Shigeta, Y. & Matsumura, H. (2017) Identification of the key interactions in structural transition pathway of FtsZ from Staphylococcus aureus. *J. Struct. Biol.* **198**, 65–73.

(68) Raymond, A., Lovell, S., Lorimer, D., Walchli, J., Mixon, M., Wallace, E., Thompkins, K., Archer, K., Burgin, A. & Stewart, L. (2009) Combined protein construct and synthetic gene engineering for heterologous protein expression and crystallization using Gene Composer. *BMC Biotechnol.* **9**, 37.

(69) Martin-Galiano, A. J., Buey, R. M., Cabezas, M. & Andreu, J. M. (2010) Mapping flexibility and the assembly switch of cell division protein FtsZ by computational and mutational approaches. *J. Biol. Chem.* **285**, 22554–22565.

(70) Miraldi, E. R., Thomas, P. J. & Romberg, L. (2008) Allosteric models for cooperative polymerization of linear polymers. *Biophys. J.* **95**, 2470–2486.

(71) Kaul, M., Mark, L., Parhi, A. K., LaVoie, E. J. & Pilch, D. S. (2016) Combining the FtsZ-Targeting Prodrug TXA709 and the Cephalosporin Cefdinir Confers Synergy and Reduces the Frequency of Resistance in Methicillin-Resistant Staphylococcus aureus. *Antimicrob. Agents Chemother.* **60**, 4290–4296.

(72) Kaul, M., Mark, L., Zhang, Y., Parhi, A. K., Lyu, Y. L., Pawlak, J., Saravolatz, S., Saravolatz, L. D., Weinstein, M. P., LaVoie, E. J. & Pilch, D. S. (2015) TXA709, an FtsZ-Targeting Benzamide Prodrug with Improved Pharmacokinetics and Enhanced In Vivo Efficacy against Methicillin-Resistant Staphylococcus aureus. *Antimicrob. Agents Chemother.* **59**, 4845–4855.

(73) Fujita, J., Maeda, Y., Mizohata, E., Inoue, T., Kaul, M., Parhi, A. K., LaVoie, E. J., Pilch, D. S. & Matsumura, H. (2017) Structural Flexibility of an Inhibitor Overcomes Drug Resistance Mutations in Staphylococcus aureus FtsZ. *ACS Chem. Biol.* **12**, 1947–1955.

(74) Stokes, N. R., Baker, N., Bennett, J. M., Chauhan, P. K., Collins, I., Davies, D. T., Gavade, M., Kumar, D., Lancett, P., Macdonald, R., Macleod, L., Mahajan, A., Mitchell, J. P., Nayal, N., Nayal, Y. N., Pitt, G. R., Singh, M., Yadav, A., Srivastava, A., Czaplewski, L. G. & Haydon, D. J. (2014) Design, Synthesis and Structure-Activity Relationships of Substituted Oxazole-Benzamide Antibacterial Inhibitors of FtsZ. *Bioorg. Med. Chem. Lett.* **24**, 353–359.

(75) Stokes, N. R., Baker, N., Bennett, J. M., Berry, J., Collins, I., Czaplewski, L. G., Logan, A., Macdonald, R., Macleod, L., Peasley, H., Mitchell, J. P., Nayal, N., Yadav, A., Srivastava, A. & Haydon, D. J. (2013) An improved small-molecule inhibitor of FtsZ with superior in vitro potency, drug-like properties, and in vivo efficacy. *Antimicrob. Agents Chemother.* **57**, 317–325.

(76) Adams, P. D., Afonine, P. V., Bunkoczi, G., Chen, V. B., Davis, I. W., Echols, N., Headd, J. J., Hung, L. W., Kapral, G. J., Grosse-Kunstleve, R. W., McCoy, A. J., Moriarty, N. W., Oeffner, R., Read, R. J., Richardson, D. C., Richardson, J. S., Terwilliger, T. C. & Zwart, P. H. (2010) PHENIX: a comprehensive Python-based system for macromolecular structure solution. *Acta Crystallogr. D Biol. Crystallogr.* **66**, 213–221.

(77) Pettersen, E. F., Goddard, T. D., Huang, C. C., Couch, G. S., Greenblatt, D. M., Meng, E. C. & Ferrin, T. E. (2004) UCSF Chimera--a visualization system for exploratory research and analysis. *J. Comput. Chem.* **25**, 1605–1612.

(78) Artola, M., Ruíz-Avila, L. B., Ramírez-Aportela, E., Martínez, R. F., Araujo-Bazán, L., Vázquez-Villa, H., Martín-Fontecha, M., Oliva, M. A., Martín-Galiano, A. J. & Chacón, P. (2017) The structural assembly switch of cell division protein FtsZ probed with fluorescent allosteric inhibitors. *Chemical Science* **8**, 1525–1534.

(79) Marquez, I. F., Mateos-Gil, P., Shin, J. Y., Lagos, R., Monasterio, O. & Velez, M. (2017) Mutations on FtsZ lateral helix H3 that disrupt cell viability hamper reorganization of polymers on lipid surfaces. *Bba-Biomembranes* **1859**, 1815–1827.

(80) Salas, P. G. D., Horger, I., Martin-Garcia, F., Mendieta, J., Alonso, A., Encinar, M., Gomez-Puertas, P., Velez, M. & Tarazona, P. (2014) Torsion and curvature of FtsZ filaments. *Soft Matter* **10**, 1977–1986.

(81) Mateos-Gil, P., Paez, A., Horger, I., Rivas, G., Vicente, M., Tarazona, P. & Velez, M. (2012) Depolymerization dynamics of individual filaments of bacterial cytoskeletal protein FtsZ. *Proc. Natl. Acad. Sci. U. S. A.* **109**, 8133–8138.

(82) Mingorance, J., Tadros, M., Vicente, M., Gonzalez, J. M., Rivas, G. & Velez, M. (2005) Visualization of single Escherichia coli FtsZ filament dynamics with atomic force microscopy. *J. Biol. Chem.* **280**, 20909–20914.

(83) Ando, T., Uchihashi, T., Kodera, N., Yamamoto, D., Miyagi, A., Taniguchi, M. & Yamashita, H. (2008) High-speed AFM and nano-visualization of biomolecular processes. *Pflug Arch Eur J Phy*

456, 211–225.

(84)   Ando, T., Kodera, N., Takai, E., Maruyama, D., Saito, K. & Toda, A. (2001) A high-speed atomic force microscope for studying biological macromolecules. *Proc. Natl. Acad. Sci. U. S. A.* **98**, 12468–12472.

(85)   Sugimoto, S., Yamanaka, K., Nishikori, S., Miyagi, A., Ando, T. & Ogura, T. (2010) AAA(+) Chaperone ClpX Regulates Dynamics of Prokaryotic Cytoskeletal Protein FtsZ. *J. Biol. Chem.* **285**, 6648–6657.

(86)   Wendel, M., Lorenz, H. & Kotthaus, J. P. (1995) Sharpened electron beam deposited tips for high resolution atomic force microscope lithography and imaging. *Appl. Phys. Lett.* **67**, 3732–3734.

(87)   Jansson, M., Li, Y. C., Jendeberg, L., Anderson, S., Montelione, G. T. & Nilsson, B. (1996) High-level production of uniformly ^{15}N- and ^{13}C-enriched fusion proteins in Escherichia coli. *J. Biomol. NMR* **7**, 131–141.

(88)   LeMaster, D. M. & Richards, F. M. (1985) ^{1}H-^{15}N heteronuclear NMR studies of Escherichia coli thioredoxin in samples isotopically labeled by residue type. *Biochemistry* **24**, 7263–7268.

(89)   Sheldrick, G. M. (2008) A short history of SHELX. *Acta Crystallogr. A* **64**, 112–122.

(90)   Pape, T. & Schneider, T. R. (2004) HKL2MAP: a graphical user interface for macromolecular phasing with SHELX programs. *J. Appl. Cryst.* **37**, 843–844.

(91)   Laskowski, R., MacArthur, M., Moss, D. & Thornton, J. (1993) PROCHECK: a program to check the stereochemical quality of protein structures. *J Appl Cryst* **26**, 283–291.

(92)   Haney, S. A., Glasfeld, E., Hale, C., Keeney, D., He, Z. Z. & de Boer, P. (2001) Genetic analysis of the *Escherichia coli* FtsZ·ZipA interaction in the yeast two-hybrid system. *J. Biol. Chem.* **276**, 11980–11987.

List of Publications

1. Expression, purification, crystallization and preliminary crystallographic study of FtsA from methicillin-resistant *Staphylococcus aureus*

   Junso Fujita, Yuma Miyazaki, Mika Hirose, Chioko Nagao, Eiichi Mizohata, Yoshimi Matsumoto, Kenji Mizuguchi, Tsuyoshi Inoue, and Hiroyoshi Matsumura

   Acta Crystallographica Section F, **69**(Pt 8), 895–898 (2013)

2. Crystal structure of FtsA from *Staphylococcus aureus*

   Junso Fujita, Yoko Maeda, Chioko Nagao, Yuko Tsuchiya, Yuma Miyazaki, Mika Hirose, Eiichi Mizohata, Yoshimi Matsumoto, Tsuyoshi Inoue, Kenji Mizuguchi, and Hiroyoshi Matsumura

   FEBS Letters, **588**(10), 1879–1885 (2014)

3. Identification of the key interactions in structural transition pathway of FtsZ from *Staphylococcus aureus*

   Junso Fujita*, Ryuhei Harada*, Yoko Maeda, Yuki Saito, Eiichi Mizohata, Tsuyoshi Inoue, Yasuteru Shigeta, and Hiroyoshi Matsumura

   Journal of Structural Biology, **198**(2), 65–73 (2017)

   *Co-first authors.

4. Structural flexibility of an inhibitor overcomes drug resistance mutations in *Staphylococcus aureus* FtsZ

   Junso Fujita, Yoko Maeda, Eiichi Mizohata, Tsuyoshi Inoue, Malvika Kaul, Ajit K. Parhi, Edmond J. LaVoie, Daniel S. Pilch, and Hiroyoshi Matsumura

   ACS Chemical Biology, **12**(7), 1947–1955 (2017)

List of Supplementary Publications

1. Active site geometry of a novel aminopropyltransferase for biosynthesis of hyperthermophile-specific branched-chain polyamine

    Ryota Hidese, Ka Man Tse, Seigo Kimura, Eiichi Mizohata, **Junso Fujita**, Yuhei Horai, Naoki Umezawa, Tsunehiko Higuchi, Masaru Niitsu, Tairo Oshima, Tadayuki Imanaka, Tsuyoshi Inoue, and Shinsuke Fujiwara

    FEBS Journal, **284**(21), 3684–3701 (2017)

Acknowledgements